

1 **Mapping and interpreting the Subcrustal Reflectivity Beneath central and**
2 **South-West Iberia**

3
4 **I. Palomeras¹, P. Ayarza¹, J. Andrés², A. M. Álvarez-Valero¹, J. Gómez-Barreiro¹, J. Díaz²,**
5 **J. Alcalde², R. Carbonell²**

6 ¹ Department of Geology, University of Salamanca, Salamanca, Spain

7 ² Institute of Earth Sciences “Jaume Almera”, ICTJA-CSIC, Barcelona, Spain

8 Corresponding author: Imma Palomeras (imma@usal.es)

9 **Key Points:**

- 10 • Lithospheric-mantle reflectors beneath the SW-Iberian Variscan Belt
11 • Synthetic modeling
12 • Spinel- to Garnet-lherzolite transition zone: the Hales gradient zone.

15 **Abstract**

16 At least two sub-Moho reflectors have been identified in different seismic refraction and wide-
17 angle reflection experiments conducted in western Iberia since the early 1990's. The kinematics
18 and wavelet characteristics of the shallowest event are probably produced by an increase in P-
19 wave velocity. Forward modeling places this velocity contrast at ~70-75 km depth beneath the
20 Ossa-Morena Zone (OMZ) shallowing up to 50-60 km beneath the Central Iberian Zone (CIZ).
21 The coda and amplitude of this arrival suggest that it can correspond to a ~10 km thick
22 heterogeneous layer. To test this hypothesis, we used a 2D second order finite-difference
23 acoustic full wave-field modeling scheme. The input model includes a layer of randomly
24 distributed bodies thinner than $\frac{1}{4}$ of the wavelength of the source waves and $\Delta V_p = \pm 0.1$ km/s at
25 the considered depth range. The resulting synthetic data reproduce well the observed amplitudes
26 and codas because of the constructive interferences caused by this heterogeneous zone. The
27 origin of this layer is also discussed here in detail, which is very likely related to the phase
28 transition from spinel to garnet lherzolite, the so-called Hales discontinuity. A second reflection
29 also observed in some of the experiments suggests the presence of a velocity inversion at greater
30 depths. Forward modeling places this discontinuity at around 90 km depth beneath the OMZ,
31 deepening to 105-110 km depth beneath the southeast CIZ, and shallowing up to 80 km depth in
32 the northeast CIZ. The observed characteristics of this event are consistent with those of the
33 lithosphere-asthenosphere boundary (LAB).

34 **Plain Language Summary**

35 The continental upper mantle is considered to be mainly peridotitic. However, this composition
36 is likely no uniform, and the seismic reflectivity observed with different seismic methods
37 suggests the presence of certain layering within the lithospheric mantle. The Western Iberia
38 (Spain) has been sampled by multiple active source seismic surveys that illuminated the
39 uppermost mantle, showing strong sub-Moho reflections. The arrival time and nature of the
40 shallowest upper mantle reflection indicates that it corresponds to a positive velocity contrast
41 placed at ~50-75 km depth (depending on the tectonic province). To reproduce the recorded coda
42 and amplitude a ~10 km thick heterogeneous layer consisting of randomly distributed bodies
43 thinner than $\frac{1}{4}$ of the wavelength of the source waves and with small velocity variations at the
44 considered depth needs to be introduced in the velocity model. The characteristics of this layer
45 (the contrast in physical properties and depth), agree with those of the transition from spinel to
46 garnet lherzolite, the so-called Hales discontinuity. The seismic datasets also recorded a second
47 deeper reflection, which origin can be attributed to a velocity decrease with depth at ~90-110 km
48 depth. Due to its characteristics and observed depth, it has been interpreted as the lithosphere-
49 asthenosphere boundary (LAB).

50 **1 Introduction**

51 Observations from field sampling (i.e. mantle xenoliths and outcrops of exhumed mantle) and
52 indirect methods (e.g. the range of measured seismic velocities) suggest that the continental
53 upper mantle is mainly peridotitic in composition. However, the mantle's composition is not
54 uniform (e.g. *Stracke, 2012*), and the significant lithological and structural heterogeneities can
55 produce impedance contrasts high enough to be observed in seismic data [*Fumagalli and*
56 *Klemme, 2015*]. The birth and evolution of new seismic techniques and the densification of

57 seismic arrays have confirmed the presence of layering within the continental lithosphere, with
58 numerous positive and negative velocity discontinuities [e.g. *Thybo and Anderson, 2006; Clowes*
59 *et al., 2010*, and references therein].

60 Seismic reflections are related to variations in the physical properties of subsurface rocks due to
61 compositional changes, phase transitions, strain state variations or anisotropy. All these scenarios
62 are capable to produce upper mantle reflections and have been invoked by several authors to
63 explain the observed reflectivity in the lithospheric mantle. One of such lithospheric reflectors is
64 the Hales discontinuity, named after *Hales [1969]*. It was observed at ~60-90 km depth because
65 of an increase in isotropic velocity. This sub-Moho positive seismic impedance ($z=V*\rho$, where z
66 is the seismic impedance, V is the seismic wave velocity and ρ is the density) contrast is
67 observed at different places around the globe by different means:, e.g., long-range controlled
68 source experiments [*Hales, 1969; Hales et al., 1980; Massé, 1987; Hajnal et al., 1997;*
69 *Musacchio et al., 2004; Ayarza et al., 2010*], shear-coupled P-waves [*Zand and Randall, 1985*],
70 ScS reverberations [*Revenaugh and Jordan, 1991*], precursors to sSH [*Zhang and Lay, 1993*],
71 receiver functions [*Bostock, 1998; Levin and Park, 2000; Saul et al., 2000*], joint inversion of
72 Rayleigh wave and receiver functions [*Anand et al., 2017*], and, most recently, autocorrelations
73 of ambient seismic noise [*Taylor et al., 2016; Andrés et al., 2018*]. The origin of this upper
74 mantle discontinuity has been addressed to (i) compositional changes related to the existence of
75 eclogitized subducted oceanic crust [*Snyder, 1991; Chian et al., 1998; Cook et al., 2004*], (ii)
76 petrological changes responding to a phase transition from spinel-garnet to garnet-only
77 peridotites [*Hales, 1969; Fernández Viejo and Clowes, 2003; Ayarza et al., 2010; Anand et al.,*
78 *2017*], and (iii) velocity anisotropy variations [*Fuchs, 1983; Bostock, 1997, 1998; Levin and*
79 *Park, 2000*]. Also, the fact that this feature is observed by controlled source seismic profiles
80 around the world, led some authors to suggest that it is a global discontinuity located at 80-100
81 km depth may exist [*Pavlenkova, 1996; Steer et al., 1998*]. Although lithospheric discontinuities
82 certainly exist, the worldwide presence of the Hales discontinuity has not been proven yet.

83 Since the early 1990's, the Iberian Massif in western Iberia (Figure 1) has been sampled by
84 multiple active source seismic surveys. These experiments employed energy sources large
85 enough to illuminate the uppermost mantle, and their results showed strong sub-Moho arrivals at
86 large offsets (>180 km) that reflect off an interface which depth concur with those assumed for
87 the Hales discontinuity. The ILIHA-DSS experiment [*Iliha DSS Group, 1993*] sampled up to
88 three different mantle reflectors in western Iberia, demarcating different azimuthal anisotropy
89 [*Díaz et al., 1993*]. The IBERSEIS-WA profiles in the southwestern Iberia [*Palomeras et al.,*
90 *2009*] showed strong uppermost mantle arrivals interpreted as the spinel- to garnet-lherzolite
91 phase transition [*Ayarza et al., 2010*]. The ALCUDIA-WA and NI (wide-angle and normal
92 incidence) seismic profiles, placed to the north of the IBERSEIS profiles, showed a number of
93 subcrustal reflections, yet, un-interpreted. In this work, we study the uppermost mantle
94 reflections imaged by all these experiments in order to produce a joint interpretation of this
95 reflectivity. Furthermore, synthetic seismic modeling is employed here to explain the particular
96 characteristics exhibited by these subcrustal features. The aim of this manuscript is hence the
97 source, defining the extension and regional-scale relevance of this upper mantle reflectivity in
98 the Iberian Massif.

99 2 Geological Setting

100 The Iberian Massif is the largest outcrop of the Variscan belt in Western Europe (Figure 1). The
 101 Variscan orogeny resulted from the collision of the Laurussia and Gondwana continents during
 102 the late Paleozoic, resulting in the closure of the Rheic Ocean [*Martínez Catalán et al.*, 2007;
 103 *Azor et al.*, 2008, 2019]. During the convergence and collision, several allochthonous terranes
 104 were involved, defining a complex suture pattern along the orogen [*Gómez Barreiro et al.*, 2010;
 105 *Ballèvre et al.*, 2014; *Martínez Catalán et al.*, 2019; *Quesada et al.*, 2019]. Later on, a
 106 transpressional tectonic regime is inferred from the structure, variably modified by gravitational
 107 re-equilibration in the hinterland and the formation of orogenic bends (oroclinals) [e.g. *Martínez*
 108 *Catalán*, 2012; *Azor et al.*, 2019]. Different tectonostratigraphic zones have been defined in the
 109 north and southwest branches of the Iberian Massif. From hinterland to foreland: a) the north
 110 branch includes the Galicia-Trás-os-Montes Zone (GTMZ), the Central Iberian Zone (CIZ), the
 111 West-Asturian Leonese Zone (WALZ) and the Cantabrian Zone (CZ); b) the southwest branch
 112 includes the southern part of the CIZ, the Ossa-Morena Zone (OMZ) and the South Portuguese
 113 Zone (SPZ) (Figure 1). Focusing on the southwest branch of the Iberian Massif, the CIZ formed
 114 part of the passive margin of Gondwana, whereas the OMZ was probably a continental terrain
 115 that had partly drifted away from Gondwana [*Fonseca and Ribeiro*, 1993; *Azor et al.*, 2008].
 116 Tectonic processes were diachronical across the belt and included several phases. An initial
 117 compression occurred during Devonian times (390-360 Ma) related to subduction/collision
 118 affected the OMZ and the southern boundary of the CIZ [*Simancas et al.*, 2003]. In the
 119 Mississippian (360-330 Ma), an extensional episode affected the SPZ, OMZ and southernmost
 120 CIZ, producing, normal faulting, basin filling, gneissic domes and mafic magmatism [*Dias da*
 121 *Silva et al.*, 2018]. A second compressional episode in the Late Mississippian-Early
 122 Pennsylvanian (330-310 Ma), and recorded in SPZ and OMZ, resulted in an inversion of basins
 123 and upright folding. A late extensional episode is observed during the late Pennsylvanian-
 124 Permian (310-280 Ma), producing normal faulting and some late-orogenic granitic magmatism.
 125 Transcurrent component, both transpression and transtension, was important during the orogeny
 126 as clearly demonstrated by the development of large wrench shear zones formed at late orogenic
 127 episodes [e.g. *Silva and Pereira*, 2004; *Martínez Catalan*, 2011].

128 The western Iberian massif has been largely stable since the end of the Permian, and Paleozoic
 129 basement rocks are exposed in the area. Crustal thickness averages 31-32 km, in the CIZ, OMZ,
 130 and SPZ, shallowing up to 29 km beneath the southern CIZ and deepening to 35 km near the
 131 Central System [*Diaz et al.*, 2016; *Palomeras et al.*, 2017] the latter being probably the result of
 132 Alpine reworking [*Ehsan et al.*, 2015; *Andrés et al.*, 2019].

133

134 3 Previous Controlled Source Seismic Surveys: the ILIHA-DSS and IBERSEIS-WA 135 Projects Results for the Uppermost Mantle

136 Three wide-angle seismic experiments have sampled the crust and upper mantle in the
 137 southwestern and western part of the Iberian Massif (Figure 1). The ILIHA-DSS experiment,
 138 acquired in the early 1990's [*Iliha DSS Group*, 1993], was a large deep seismic sounding
 139 experiment designed to study the uppermost mantle (from 30 to ~100 km depth) of the entire
 140 Iberian Massif. It consisted of a set of 6 wide-angle transects across the Iberian Peninsula, with
 141 station spacing of 5-10 km on average. The source employed consisted of 500 to 1000 kg of
 142 explosives fired offshore at the edges of the profiles. In this paper, we focus on the four transects

143 that cross through the study area: Line BX, Line DA, line BE, and Line CF (Figure 1). These
144 transects, three of them reversed and one unreversed, present offsets larger than 600 km and
145 sample the Iberian Massif lithosphere at different azimuths. The ILIHA-DSS analysis indicated
146 the presence of 3 sub-Moho reflectors beneath southwest Iberia [*Iliha DSS Group*, 1993] at 45,
147 68 and 88 km depth. They define a layered mantle lithosphere with differentiated P-wave
148 velocity and azimuthal anisotropy [*Díaz et al.*, 1993].

149 A decade later, the IBERSEIS project was launched with the aim of acquiring high-resolution
150 seismic data in the lithosphere of southwest Iberia. One normal incidence (NI) and two wide-
151 angle (WA) profiles were acquired between 2001 and 2003. The IBERSEIS-NI was a ~300 km
152 long normal incidence reflection experiment that crossed, from south to north, the SPZ, the
153 OMZ, the CIZ, and their respective sutures, providing a detailed crustal image [*Simancas et al.*,
154 2003]. The profile, with a station and vibration point spacing of 35 m and 70 m respectively,
155 exhibited a reflective crust with a clear reflection at its base, but a seismically transparent mantle
156 [*Simancas et al.*, 2003; *Ayarza et al.*, 2010]. To further investigate the nature of the crustal
157 layers, two wide-angle reflection/refraction transects (IBERSEIS-WA) were also acquired
158 [*Palomeras et al.*, 2009]. Transect A overlapped the IBERSEIS-NI section and Transect B sat
159 west from Transect A, sharing its northern edge (Figure 1). Transect A was 330 km long with a
160 station spacing of ~400 m. Transect B was ~300 km long with a station spacing of ~150 m. Six
161 shots spaced ~60 km were located along both transects. However, the three northernmost ones on
162 Transect A failed. Contrarily to what the IBERSEIS-NI results show, both transects present clear
163 sub-Moho reflections at large offsets (>180 km): *e.g.*, in shots 2 and 3 on Transect A, and shots 1
164 and 6 on Transect B [*Ayarza et al.*, 2010]. These reflections were first interpreted as an interface
165 at 65-70 km depth featuring a V_p contrast from 8.3 km/s to 8.5 Km/s [*Palomeras et al.*, 2009].
166 *Ayarza et al.* [2010] modeled this phase and found that, to reproduce the observed high
167 amplitudes and arrival times, the phase must reflect off from a ~10 km thick band located at ~60-
168 70 km depth, containing ~150 m wide heterogeneities and being characterized by a velocity
169 increase from 8.2 to 8.3 km/s. These attributes are aligned with the overall characteristics
170 predicted for the spinel- to garnet-lherzolite phase transition, the so-called Hales discontinuity.

171 As stated above, despite strong reflections from the mantle are observed in the IBERSEIS wide-
172 angle reflection/refraction surveys, no upper mantle reflectivity is identified in the IBERSEIS-NI
173 transect. *Ayarza et al.* [2010] outlined four possible reasons that might explain this contrasting
174 seismic signature in both coincident datasets: 1) the impedance contrast of this interface is not
175 strong enough and needs a tuning effect not met with the vertical incidence seismic frequencies;
176 2) the reflection coefficients at low incidence angles are lower than at wide-angle higher
177 incidence angles; 3) vertical incidence data is less sensitive to gradient zones such as the
178 modeled Hales discontinuity; and/or 4) mid-point projections of both data sets do not exactly
179 coincide and thus, they might not be sampling the same exact area.

180 **4 The ALCUDIA Experiment**

181 The ALCUDIA experiments were designed to image the CIZ to the northeast of the previous
182 IBERSEIS profiles. The ALCUDIA project also included two seismic acquisition experiments:
183 1) the ALCUDIA-NI, a ~250 km-long normal incidence profile across the CIZ [*Martínez*
184 *Poyatos et al.*, 2012], and 2) the ALCUDIA-WA, a ~300 km long wide-angle
185 reflection/refraction profile that overlaps the ALCUDIA-NI [*Ehsan et al.*, 2015].

186 4.1. ALCUDIA-NI Data and Results

187 The ALCUDIA-NI is a high-resolution normal incidence profile with a 35 m station spacing
 188 and a vibration point spacing of 70 m. The acquisition parameters and processing flow are
 189 described in detail in *Martínez Poyatos et al.* [2012]. The high-resolution section provides a
 190 detailed image of the crust with a clear Moho discontinuity at 10 s two-way travel time
 191 (twtt), c. ~30km depth. Contrarily to the IBERSEIS-NI section and despite having exactly the
 192 same acquisition parameters, the ALCUDIA-NI imaged ~20 km-long sub-horizontal
 193 continuous strong reflectors at 16 and 19 s twtt in the central and northern part of the profile,
 194 beneath common depth points (CDP) ~1000 to ~2000 and ~6200 to ~7000 respectively
 195 [*Martínez Poyatos et al.*, 2012] (Figure 2). Assuming a crustal velocity of 6 km/s and a
 196 mantle velocity of 8.0 km/s [*Ehsan et al.*, 2015], these reflectors correspond to an interface at
 197 54 km depth to the north, below CDP 1000-2000, and at 66 km depth at the center, below
 198 CDP 6200-7000. However, there is no interpretation to date for these features.

199 4.2. ALCUDIA-WA: Data Analysis and Modeling

200 The design of the ALCUDIA-WA profile mimics that of the IBERSEIS-WA: five shot points
 201 located ~70 km apart along the ~300 km-long transect with station spacing of 350-400 m
 202 [*Ehsan et al.*, 2015]. The experiment was aimed to provide the P-wave velocity distribution
 203 of the lithosphere in the CIZ. The large offsets of shot gathers A1, A4 and A5 allow the
 204 identification of deep arrivals indicating the presence of sub-Moho reflectors in the region.
 205 These reflections are, as yet, un-interpreted and only crustal models have been published up
 206 to date.

207 Since the goal of this manuscript is to model the uppermost mantle structure in western
 208 Iberia, and the ALCUDIA-WA crustal phases have been already modeled [*Ehsan et al.*,
 209 2015], we just focus on sub-crustal arrivals. Different processing flows and parameters were
 210 tested in the shot gathers to improve the coherency of the signal and to facilitate
 211 identification of different phases in the upper mantle. In this study we also present shot
 212 gather A1 that was not included in the crustal modeling presented by *Ehsan et al.* [2015].
 213 Picked arrivals will be labeled as follows: Pn for the head wave traveling within the upper
 214 mantle, PmP for the P-wave reflected at the base of the crust (Moho), and PM_iP for the upper
 215 mantle reflected phases, where i represents the phase (i.e. 1 or 2).

216 Several upper mantle reflections are observed in shot gathers 1, 4, and 5 of the ALCUDIA-
 217 WA (Figure 3). A strong arrival is seen in ALCUDIA shot 1 at large offsets (>190 km) and
 218 ~7 s (hereafter, reduced time, reduction velocity=8 km/s). It features higher amplitudes than
 219 Pn and can be followed up to 250 km offsets. This arrival presents a conspicuous coda of ~1
 220 s (Figure 3, PM₁P phase) that mimics the one observed in the IBERSEIS-WA shot gathers at
 221 similar offsets and times [*Ayarza et al.*, 2010]. ALCUDIA shot 4 presents an arrival at ~190
 222 km offset and 10 s that extends along ~25 km with very high amplitudes. This phase has
 223 similar characteristics to the PM₁P phase on shot 1, with similar ~1s-long coda and it has
 224 been labeled as PM₁P in Figure 3 as well. Another set of deeper discontinuous reflections is
 225 observed in shots 4 and 5 at offsets greater than 150 km and between 13 and 14 s twtt (Figure
 226 3, PM₂P).

227 To understand these subcrustal arrivals, we first tested if they could correspond to a P-to-S
 228 wave conversion at the Moho discontinuity (i.e. the PmS phase) or vice versa (i.e. the SmP

229 phase). For a 30 km-thick crust with average P- and S-wave velocities of 6 and 3.6 km/s
230 respectively, the PmS/SmP phase would arrive at 46.40 s twtt at 200 km offset, or 21.40 s at
231 a reduced velocity of 8 km/s. The sub-Moho arrivals that are under study in this manuscript
232 arrive much earlier than these theoretical times, thus rejecting the hypothesis that they
233 correspond to converted waves.

234 A spectral analysis has been carried out in order to better study the attributes of these phases.
235 The dominant frequency of the PM₁P phase is in the range of 10-20 Hz (Figure 4a and 4b),
236 whereas the PM₂P phase, has its highest amplitudes at a lower frequency range (< 10 Hz,
237 Figure 4c and 4d). According to these results, a bandpass filter of 5-20 Hz was applied to the
238 data with the goal to enhance the image of both phases.

239 A further analysis step focused on the polarity of the phases, which provides information
240 about the impedance contrast (positive or negative) of the interfaces that generate the
241 reflections. We compared the polarity of subcrustal reflections with that of the PmP phase,
242 whose polarity responds to an impulsive source reflected off a positive impedance contrast
243 (crust to mantle). Accordingly, we stacked traces that encompass both reflections and
244 compared the resulting wiggle with the one obtained from stacking PmP arrivals (Figure 5).
245 Stacking of PM₁P arrivals of shots 1 and 4 result in a reflection with the same positive
246 polarity than the PmP arrival, indicating that the PM₁P phase most likely reflects off an
247 interface that features an increase in seismic impedance (V_p and ρ) with depth. On the other
248 hand, the stack of deeper PM₂P reflections observed in shots 4 and 5 into single traces shows
249 that their polarity is negative, the opposite to that observed in the PmP.

250 Once the above-mentioned reflections were attributed to contrasting impedance variations,
251 mantle reflections were modeled using the ray-tracing based utilities by *Zelt and Smith*
252 [1992], taking into account that the crustal structure of the area sampled by the ALCUDIA
253 experiment is well constrained [*Martínez Poyatos et al.*, 2012; *Ehsan et al.*, 2014, 2015]. The
254 work presented in this manuscript extends the crustal velocity model of *Ehsan et al.* [2015]
255 into the upper mantle resulting in a 2D P-wave velocity structure down to 120 km depth
256 (Figure 6).

257 The positive polarity of the PM₁P phase is considered to be related to an increase in V_p . The
258 characteristics of this phase (~1s-long coda and high-amplitude) are similar to the ones
259 observed in the IBERSEIS-WA profiles [*Ayarza et al.*, 2010], where the amplitudes and coda
260 observed can be reproduced by a ~10 km thick heterogeneous gradient zone (from 8.2 to 8.3
261 km/s) with small V_p variations (contrast < 1%). Accordingly, the same gradient zone is
262 proposed as the source of this uppermost mantle reflection. The shallowest observed part of
263 the gradient zones is around ~ 51 km depth to the south of the ALCUDIA-WA section and
264 deepens to 57 km depth to the north. The velocity increase from 8.2 to 8.3 km/s in an
265 approximately 10 km thick band provides us with an interface whose characteristics and
266 travel time coincide with those of PM₁P. On the other hand, the PM₂P phase, which presents
267 inverse polarity when compared with PmP, corresponds to a decrease in V_p from 8.3 to 8.0
268 km/s on an interface located at 100 km depth that sinks to 113 km depth to the north (Figure
269 6). Although some of the observed reflections are not continuous enough to be considered
270 profile-long structures, they have been modeled as such for computational reasons. We will
271 discuss the nature of these reflectors in the following sections.

272 5. ILIHA-DSS Modeling

273 In this paper, the P-wave velocity models from the ILIHA-DSS experiment [*Iliha DSS Group*,
 274 1993] are reevaluated in the light of the new high resolution IBERSEIS-WA and ALCUDIA-
 275 WA data and crustal models. Previous lithospheric models interpreted up to three high amplitude
 276 subcrustal phases as alternating thin (<5 km thick) low-velocity layers with high-velocity ones in
 277 the uppermost mantle. This layered geometry was necessary to produce an impedance contrast
 278 high enough to reproduce the observed amplitudes. When such low-velocity layers (7.7 km/s) are
 279 included in the model, the underlying high velocities need to reach up to 8.6 km/s in order to fit
 280 both amplitudes and travel times. However, such high velocities are not expected at depths
 281 shallower than ~300 km according to the IASP91 and AK135 1D Earth velocity-depth models
 282 [*Kennett and Engdahl*, 1991; *Kennett et al.*, 1995]. Furthermore, studies on the estimation of
 283 lithospheric mantle properties based on the petrological analysis in xenoliths indicate that at 100
 284 km depth, P-wave velocity beneath tectons (areas where the crust was formed or modified not
 285 later than 1Ga) is in the range of 8.20-8.25 km/s [*Griffin et al.*, 2009]. In order to reconcile the
 286 observed phases and the models with the estimated velocity from these petrological studies, we
 287 have tried to adjust the observed ILIHA experiment travel times with lower (< 8.4 km/s) P-wave
 288 velocities, in better agreement with the IBERSEIS-WA and ALCUDIA-WA results. As observed
 289 in these profiles, the ILIHA high amplitudes and coda can be recovered considering the tuning
 290 effect produced by a gradient heterogeneous zone. Following this strategy, we have performed
 291 forward modeling using the same code [*Zelt and Smith*, 1992] to obtain the velocity distribution
 292 along the four transects presented here: lines BX, DA, BE, and CF (Figures 1 and 7). The crustal
 293 part of the models include the results of the IBERSEIS-WA and the ALCUDIA-WA experiments
 294 for each of the Variscan tectonic zones, thus having well constrained velocity and structure at
 295 that level. Similarly, to the IBERSEIS-WA and ALCUDIA-WA datasets, we assumed that the
 296 shallowest arrival (PM₁P) is produced by a positive impedance contrast resulting from a ~10 km
 297 thick heterogeneous gradient zone (P-wave velocity increases from 8.2 km/s to 8.3 km/s). For a
 298 closer inspection of the identified phases, the reader is referred to *Iliha DSS Group* [1993]

299 5.1. Line DA

300 Line DA is an unreversed ~720 km-long line, hence only shot D1 is analyzed (Figures 1 and
 301 7a). Two phases were picked by the *Iliha DSS Group* [1993]. A first clear arrival appears at
 302 230-400 km offset and 8.0 s twtt. This phase has a wave coda of ~1 s twtt. A second arrival is
 303 identified at 390 km offset and 8 s twtt. Forward raytracing modeling indicates that the first
 304 arrival (PM₁P) corresponds to a reflector placed at 75 km depth beneath the OMZ (Figure
 305 7a). The second arrival is modeled as an interface at 90 km depth beneath the OMZ-CIZ with
 306 a P-wave velocity decrease from 8.3 to 8.0 km/s.

307 5.2. Line BX

308 Two shots were fired for reversed line BX, one at each edge of the ~680 km-long profile
 309 (Figures 1 and 7b). Three separated arrivals were picked for shot B2 [*Iliha DSS Group*,
 310 1993]. The shallowest one (PM₁P) is observed from 240 to 390 km offset and 6.5 s twtt. A
 311 second arrival is identified at 350 km offsets and 7 s twtt. A later arrival is picked at 420 km
 312 offset and 7.5 s (PM₂P). On the other edge, shot X2 presents also three upper mantle arrivals:
 313 at ~7 s and offsets of 200 km (PM₁P), at 8 s and 280 km offset, and at 8 s twtt and 440 km
 314 offset (PM₂P). The shallowest arrivals have thus been modeled as a reflector at 62 km depth

315 to the north (beneath the western part of the CIZ) that shallows up to 60 km to the south
 316 (beneath the OMZ and the Guadalquivir basin). The second interface is modeled as reflected
 317 from an interface at 72 km depth beneath the western part of the CIZ and 84 km depth
 318 beneath the OMZ, that could correspond to a lower part of the modeled gradient zone. The
 319 deepest interface is modeled to adjust the later arrivals from shots B2 and X2. These match
 320 the travel time of reflections off an interface placed at 95-100 km depth with a decrease in
 321 velocity with depth from 8.3 to 8.0 km/s (Figure 7b).

322 5.3. Line CF

323 This reversed ~1220 km-long line presents two upper mantle arrivals on shot C [*Iliha DSS*
 324 *Group*, 1993]. A strong arrival is observed at ~270 km offset and ~7s twtt (PM₁P). As in the
 325 other lines, this sub-Moho arrival has a ~1s length wave coda. Forward modeling indicates
 326 that this arrival originates at an interface at 72 km depth beneath the OMZ (Figure 7c). A
 327 second arrival is observed at 440 km offset and 7.5 s twtt (PM₂P). This phase is modeled as a
 328 reflection coming up from an interface placed at 90 km depth beneath the CIZ (Figure 7c).
 329 Like in line BX, a decrease in velocity with depth from 8.3 to 8.0 km/s is proposed.

330 5.4. Line BE

331 This line extends for more than 900 km from west to east across the Iberian Peninsula
 332 (Figures 1 and 7d). Shot B1 recorded two sub-Moho arrivals [*Iliha DSS Group*, 1993]. A
 333 shallow arrival is identified at 200 km offset and 6.5 s twtt (PM₁P). This interface is modeled
 334 at 55 km depth beneath the northern part of the CIZ and corresponds to the top of the
 335 gradient zone. A second arrival observed at 380 km offset and 7 s twtt is modeled as reflected
 336 from an interface placed at 80 km depth beneath the same area of the CIZ (Figure 7d). Again,
 337 it corresponds to a decrease in the P-wave velocity with depth.

338 The new velocity models obtained from the ILIHA dataset do not require the existence of high-
 339 and low-velocity zones to fit the observed arrivals. Instead, a more reasonable gradient velocity
 340 zone with velocity ranges of 8.2 to 8.3 km/s and a negative velocity contrast between 8.3km/s
 341 and 8.0 km/s can reproduce the observed arrival times. Even though, in this case, we cannot
 342 recover the polarity of reflections, the modeling results indicate that these come from interfaces
 343 with similar origins to those imaged in the IBERSEIS-WA and ALCUDIA-WA and that
 344 therefore represent the same features. Our new models (Figure 7) locate the three upper mantle
 345 discontinuities deeper than in previous velocity models [*Iliha DSS Group*, 1993].

346 6. Discussion

347 Three wide-angle experiments recorded from the 1990s to 2012 imaged at least two sub-Moho
 348 reflectors in the southern and western part of the Iberian Massif. The shallowest reflector (PM₁P)
 349 has been modeled as a gradient zone where velocities increase from 8.2 to 8.3 km/s with depth.
 350 The top of this gradient zone appears at different depths beneath each of the tectonic zones
 351 (Figure 8). It is placed at ~58 km depth beneath the OMZ-SPZ junction, around the Guadalquivir
 352 Basin (GB) (see ILIHA line BX, Figure 7b), whereas in the northern and central parts of the
 353 OMZ it is in the range of 67.5 to 75 km depth. Beneath the CIZ, the shallowest reflector rises to
 354 50-62 km depth.

355 The deepest reflector (PM₂P) features a decrease in V_p with depth from 8.3 to 8.0 km/s, and its
 356 location and geometry are also variable across the different tectonic zones (Figure 8). Beneath

357 the OMZ it is located at 90 km depth (ILIHA line DA and CF, Figure 7a and c), deepening to the
 358 south down to 100 km depth (ILIHA line BX, Figure 7b). On the other side, this interface
 359 presents a variable topography beneath the CIZ. The ALCUDIA-WA survey images this
 360 interface at 105-110 km depth (Figure 6) beneath its southeastern part, meanwhile further to the
 361 northwest it shallows up to 80 km depth (ILIHA line BE, Figure 7). The variable topography of
 362 both interfaces and its nature are discussed in the following sub-section.

363 6.1. Characteristics of the SW-Iberia Sub-Moho Subcritical Reflection, PM₁P

364 We sampled the shallower reflector PM₁P by three different wide-angle reflection surveys. It
 365 appears to exist below the OMZ and CIZ in the wide depth range of 50-75 km. This
 366 boundary produces reflections at large offsets and it is observed discontinuously as a few tens
 367 of kilometers feature. In addition, a similar reflective pattern is observed in the ALCUDIA-
 368 NI (normal-incidence) profile, where ~20 km long mantle reflections are imaged between
 369 ~16 and ~19 s twtt (Figure 2). A recent seismic transect imaging northwest and central Iberia
 370 using ambient noise autocorrelation [Andrés *et al.*, 2018] and Global-Phase Seismic
 371 Interferometry [Andrés *et al.*, 2019] has shown the presence of upper mantle reflectors
 372 beneath the Duero Basin and the Central System at similar depths: 12-13 s and 15 s twtt for
 373 the shallowest reflector, and a second deeper one at 18 s twtt beneath the Duero Basin. As
 374 these reflections are not continuous in any of the studied datasets, we cannot state that they
 375 represent a single, orogen-scale interface extending below the entire CIZ and OMZ.
 376 However, some considerations should be made regarding this point. The Fresnel zone
 377 contributes to the formation of the reflected wave fields determining the minimum size of a
 378 structure that can be resolved. The size of the Fresnel zone, and hence the seismic resolution,
 379 is strongly dependent on the dominant frequency and depth. The dataset used in this study
 380 has a dominant frequency of around 10 Hz for the PM₁P phase, which implies a lateral
 381 resolution of 3.5-4 km at depths of 60 km. Moreover, the P-wave reflectivity response from
 382 autocorrelation of ambient noise studies carried out in this region by Andrés *et al.* [2018], use
 383 dominant frequencies of 4 Hz, which implies Fresnel zones of around 7.8 km at the same
 384 depth. This indicates that subsurface zones smaller than these values cannot be individualized
 385 or even detected by the experiments presented here, establishing a minimum lateral extent for
 386 the modeled feature. Accordingly, several possibilities exist for the geometry of this
 387 reflector: (i) it is characterized by sets of a few km-long (15-20 km) flat features distributed
 388 heterogeneously below the OMZ and CIZ at 50-75 km depth range; or (ii) it is a more or less
 389 laterally continuous gradient zone with variable characteristics that result in a layered pattern
 390 that produces discontinuous reflectivity depending on incidence angles, wavelengths and,
 391 accordingly, development of reverberating mechanisms. It is noteworthy that although high-
 392 angle reflections in wide-angle experiments are expected, the phases analyzed here
 393 correspond to sub-critical reflections. At these angles, reflection coefficients are higher than
 394 at vertical incidence but lower than those at critical and supercritical angles [Aki and
 395 Richards, 2002] and therefore, less energy is reflected off the interfaces, making such
 396 features difficult to be observed.

397 The sub-Moho reflections in the ALCUDIA-WA (Figure 3), IBERSEIS-WA and the ILIHA-
 398 DSS shot records show a distinctive high amplitude, ~1 s long, coherent coda. Multiple
 399 similar sub-Moho reflections with a complex coda have been recorded around the world [e.g.
 400 Morozov *et al.*, 1998; Nielsen *et al.*, 2003; Carbonell, 2004; references in Clowes *et al.*,
 401 2010]. The signal characteristics of these arrivals have been linked to two potential causes:

402 (i) scattering in the crust that is enhanced through refracted multiples in a positive velocity
403 gradient mantle [Morozov *et al.*, 1998; Morozov and Smithson, 2000]. These authors
404 interpreted the long coda of the teleseismic Pn phase that is observed as a sub-Moho arrival
405 as a ‘whispering-gallery wave’ traveling within the uppermost mantle. However, neither the
406 phase, arrival times nor the offsets observed in the SW Iberia wide-angle reflection/refraction
407 data agree with these observed by the authors. (ii) Multiple reflections and scattering within a
408 heterogeneous upper mantle [Thybo and Perchuc, 1997; Fuchs *et al.*, 2002; Carbonell, 2004;
409 Ayarza *et al.*, 2010]. These authors interpret reverberations by randomly distributed
410 heterogeneous bodies with velocity fluctuations in the range of 1-2 %. The size of these
411 heterogeneities is in the range of 20-40 km long and 0.15-2 km thick, depending on the
412 authors. In some cases, a fabric of 1-2 km thick heterogeneities, with a small velocity
413 contrast ($<\pm 0.1$ km/s) needed to be included in their models to reproduce the observed coda
414 [Hammer and Clowes, 2004]. Ayarza *et al.* [2010] already modeled the sub-Moho arrivals
415 observed in the IBERSEIS-WA shot gathers as reflections coming from a ~10-11 km thick
416 heterogeneous gradient zone at 60-70 km depth below the OMZ. These authors proved that
417 the observed signal could be reproduced by a gradient zone located at uppermost mantle
418 depths with a total velocity contrast of 1.3%, from 8.2 to 8.3 km/s. The size of the random
419 heterogeneities had to be around 150 m thick in order to produce constructive interferences at
420 the dominant frequency of their dataset. The resulting synthetic seismograms reproduced the
421 offset, time, amplitudes and the ~1 s thick coda. Since the ILIHA-DSS and ALCUDIA-WA
422 sample the same area and the shallowest subcrustal arrivals show the same characteristics
423 than these observed in the IBERSEIS-WA dataset, we suggest that a stochastic distribution of
424 elliptical/elongated bodies is the likely cause of the SW-Iberia lower lithosphere reflections.
425 As the velocity contrast from 8.2 to 8.3 km/s is not high enough to produce the high
426 amplitude of the observed reflections, constructive interferences are needed to achieve phases
427 with the observed amplitudes, higher than those of Pn in some shot gathers (Figure 3). Thus,
428 a band of heterogeneities around 150-200 m in thickness extending from 55 km to 85 km
429 depth with a velocity contrast of less than 1% may be a realistic model. When the thickness
430 of the layering differs from the one proposed here, the reflector is simply not visible in our
431 datasets, thus appearing as a discontinuous feature.

432 6.2. Synthetic Modeling of PM₁P and PM₂P

433 Models in Figures 6 and 7 represent an averaged P-wave velocity distribution that fits the
434 picked travel times, but does not take into account the reflectivity. In order to reproduce it,
435 the modeling needs to consider the full propagation of an elastic P-wave. To that end, we
436 have built a ~420 km-long reference P-wave velocity model for the southern Iberian
437 lithosphere. The P-wave velocity distribution of the IBERSEIS-WA is used for the SPZ and
438 OMZ, and the one obtained from the ALCUDIA-WA results is adopted for the CIZ. Two ~15
439 and ~2 km thick heterogeneity zones are included, one at the depth of occurrence of the
440 PM₁P reflection and the other at the base of the crust, respectively (Figure 9b). Within these
441 bands, velocity fluctuations in the range ± 0.1 km/s are randomly distributed following a 2.7
442 fractal dimension [Holliger and Levander, 1992] (Figure 9b). This self-similar bimodal
443 velocity distribution is considered to be a good approximation to the structural complexity of
444 the lower crust observed in exposed cross-sections [Holliger and Levander, 1992]. The
445 horizontal and vertical correlation length of the heterogeneities are 3 km and 250 m
446 respectively.

447 Five synthetic shot gathers were calculated using a 2D second-order explicit finite-difference
448 scheme [Zahradník *et al.*, 1994] with absorbing boundary conditions at the sides and bottom
449 of the model [Sochacki *et al.*, 1987]: one at each edge of the profile (shots A and E) and three
450 along the line at km 150 (shot B), 212 (shot C), and 353 (shot D) (Figure 9d). A minimum
451 phase Ricker wavelet with a dominant frequency of 8 Hz is used to simulate the energy
452 source. The resulting shot gathers, with a trace spacing of 300 m, are presented in Figures 9c,
453 d, e and f. The primary phases (Pg, PmP, Pn, PM₁P, PM₂P) are clearly recognizable, and
454 have been labeled accordingly. Next, we will focus on the description of PM₁P and PM₂P
455 phases that are the focus of this study.

- 456 • Synthetic shot A (Figure 9d) corresponds to shot 6 of the IBERSEIS-WA Transect B
457 [Ayarza *et al.*, 2010] (Figure 9c). The Moho discontinuity is clearly imaged, including a
458 good recovery of the high amplitudes observed in the field data. The prominent PM₁P
459 phase observed in the IBERSEIS-WA shot at ~193 km offset and 8.0 s (velocity of
460 reduction of 8.0 km/s) is reproduced on the synthetic shot A with the ~1 s coda, although
461 it features a slightly lower amplitude. Synthetic shot A also presents a clear PM₂P phase
462 at ~13 s and 190 km offsets. Although this phase was not modeled for the IBERSEIS-WA
463 transects in previous works, shot 6 (IBERSEIS-WA Transect B) successfully presents an
464 arrival at the same time and offset, that we interpret as PM₂P.
- 465 • Synthetic shot B corresponds to the ALCUDIA-WA shot 1 (Figure 9c). Shot B presents a
466 clear Pn phase and the base of the crust reflection (PmP phase), both observed in the field
467 data but with lower amplitudes. The PM₁P phase is reproduced in arrival time and offsets,
468 although with lesser energy than the observed in the field data.
- 469 • Synthetic shot C corresponds to shot gather 1 of the IBERSEIS-WA Transect B (Figure
470 9). This synthetic shot presents a higher energy Pn phase than that observed in the field
471 data. On the other side, the synthetic PmP phase reproduces well the arrival time,
472 amplitudes, and thickness of the reflective package observed in the field data. Like in the
473 previous shots, the PM₁P phase mimics the one observed in the shot 1 (IBERSEIS
474 Transect B) in arrival time, offset, and coda, but with lesser energy. The PM₂P phase
475 observed in the synthetic shot C, at ~13 s at 200 km offsets, is also observed in the
476 IBERSEIS-WA shot, despite it was not interpreted and modeled previously.
- 477 • Shot D corresponds to shot 5 of the ALCUDIA-WA transect (Figure 9). Its prominent
478 PM₁P phase is not clearly observed in the synthetic. However, the PM₂P is clearly visible
479 on the synthetic shot at the expected arrival time and offsets. This phase is only visible at
480 large offsets on the field data. This pattern is also reproduced by the synthetic shot where
481 the energy reflected from the base of the lithosphere increases with offset (large reflection
482 angles and thus, larger coefficients).
- 483 • Finally, synthetic shot E emulates the ALCUDIA-WA shot 6 (Figure 9). The reflection
484 (PmP) and refraction (Pn) from the Moho discontinuity recover the arrival time,
485 amplitudes and coda observed on the field shot gather. The weak PM₁P arrival observed
486 in shot 5 is also reproduced on the synthetic shot. In the same way, the prominent PM₂P
487 phase observed at ~13 s and -270 km offset is identified at the same time and offset on the
488 synthetic shot E. Again, the synthetic and real shot gathers present higher energy at larger
489 offsets for this phase.

490 As a summary, the Moho discontinuity is clearly imaged in the five shot-gathers, reproducing
 491 the PmP phase recorded on the field data. The synthetic shots also reproduce the observed
 492 characteristics of the sub-Moho recorded phases, where the amplitude levels are achieved by
 493 constructive interferences. These observations support our model of a gradient zone with
 494 heterogeneities extending from 70 to 85 km depth beneath the SPZ and OMZ and from 55 to
 495 70 km depth beneath the CIZ as source of PMIP. The total a velocity contrast of this gradient
 496 zone is less than 1%. is the most realistic model.

497 6.3. What Do SW-Iberia Sub-Moho Reflections Represent?

498 The normal incidence profile ALCUDIA [*Martínez Poyatos et al., 2012*] images a set of sub-
 499 Moho reflections at ~18-20 s twtt at CDP 6000 to 7500 (km 100 to 130) and at ~14-17 s twtt
 500 at CDP 50 to 200 (km 10 to 40) (Figure 2). These reflections correspond to depths of 66 to 70
 501 km and 46 to 58 km depth respectively, assuming an average V_p of 6 km/s for the crust and 8
 502 km/s for the lithospheric mantle. Since the late '80s, numerous upper mantle reflectors have
 503 been reported from normal incidence profiles beneath many areas of the world [*Steer et al.,*
 504 1998 and references therein]. Different hypotheses have been invoked to explain their
 505 reflectivity: such as remnants of subducted oceanic lithosphere [*Warner et al., 1996; Balling,*
 506 2000; *Hansen and Balling, 2004; Clowes et al., 2010*], deformation fabric related to
 507 subduction [*Als Dorf et al., 1996; Abramovitz et al., 1998*], or occurrence of fluids, and mafic
 508 layering [*Warner and McGeary, 1987*]. To our knowledge, upper mantle reflections observed
 509 in normal incidence profiles have never been interpreted as a mineral phase transition. Next,
 510 we are going to consider the probability for these interpretations to match our data.

511 Reflections related to subducted slabs and to their deformation fabrics typically have certain
 512 dip. In ancient subduction zones, dipping upper mantle reflections have been often attributed
 513 to eclogitized remnants of subducted oceanic crust [*BABEL Working Group, 1990; Snyder*
 514 *and Flack, 1990; MONA LISA Working Group, 1997; Chian et al., 1998; Cook et al., 1999;*
 515 *Gorman et al., 2002*]. The transformation of mafic crust into eclogite frequently has a spread-
 516 out character, that is, stochastic [e.g. *Austrheim et al., 1997; Medaris et al., 2018*]. As our
 517 wide-angle signal indicates that a random distribution of heterogeneities is needed to
 518 reproduce the observed signal, we considered the possibility of embedded eclogitic slabs as a
 519 source of the reflectivity, a feature already observed in peridotitic massifs at different scales
 520 [e.g. *Brastad, 1983; Fountain et al., 1994; Janák et al., 2004; Shi et al., 2010; Angiboust et*
 521 *al., 2012; Renedo et al., 2015; Medaris et al., 2018*]. *Hansen and Balling [2004]* reproduced
 522 the wide-angle wavefield for a randomly eclogitized slab. Their results show that for a 50%
 523 eclogitized slab with variations in V_p of 10%, a high amplitude scattering is observed as
 524 coming from the slab. Normal-incidence sections that image old subduction zones usually
 525 show a marked Moho topography with thickened crust and Moho offsets where dipping
 526 reflectors leave the crust-mantle boundary. In our profiles, a south-dipping reflection is
 527 observed in the ALCUDIA-NI seismic image just below the Moho on CDP 10000-11000
 528 (Figure 2) but it does not comprise a significantly irregular Moho topography or a thickened
 529 crust. This featured crust-mantle wedge has been interpreted as a crocodile-like structure that
 530 accounts for ~30 km shortening at a lower crust level [*Martínez Poyatos et al., 2012*],
 531 probably imaging an imbrication of different tectonic zones during the Variscan orogeny.
 532 This amount of lower crustal shortening matches that estimated at upper crustal level. That,
 533 together with the limited lateral extent and dip of this reflection and the existence of late
 534 tectonic transpression in the area preclude a direct correlation with the sub-horizontal and

535 heterogeneous reflector modeled from our wide-angle data. In addition, the length of the
536 modelled feature (PM₁P source) exceeds that of the shortening underwent by the area during
537 the Variscan orogeny, thus hindering any relation with a Variscan subduction-related event.
538 However, the presence of eclogites, both in the OMZ-CIZ boundary [Gómez-Pugnaire *et al.*,
539 2003; Sánchez-Vizcaíno *et al.*, 2003; Pereira *et al.*, 2010] and the CIZ [Barbero and
540 Villaseca, 2000], compatible with the depth at which the reflector is located, together with
541 the late gravitational collapse underwent by of the Variscan orogen and the later
542 transpressional tectonics [Azor *et al.*, 2019] could result into truncated sub-horizontal
543 features [Aulbach *et al.*, 2017] that could be the source of mantle reflectivity, probably of a
544 more limited extent.

545 It is widely accepted that shear zones and faults can generate seismic reflectivity [e.g.
546 Fountain *et al.*, 1984; Vissers *et al.*, 1991, 1995; Calvert, 2004; Zucali *et al.*, 2014; Gómez
547 Barreiro *et al.*, 2015; Gomez Barreiro *et al.*, 2018]. Accordingly, compressional and
548 extensional events occurring in the area from the Devonian to the Late Carboniferous or even
549 Permian (depending on the area), affected the crust and may have left an imprint at the upper
550 mantle level. In collisional contexts, geodynamic modeling typically shows that the strain
551 localization produces approximately 45° dipping almost linear shear bands [Frederiksen and
552 Braun, 2001]. However different and more complex geometries could appear when orogenic
553 gravitational collapse and transpressive tectonics postdate initial subduction-collision
554 architecture [e.g. Azor *et al.*, 2019]. Again, wide-angle modeling and normal incidence
555 images for SW-Iberia do not show important upper-mantle dipping reflectors. In addition,
556 seismic images acquired in western Iberia do not show any tectonic feature offsetting the
557 Moho, *i.e.* the crust-mantle boundary seems to have acted as a rheological discontinuity.
558 Furthermore, crustal shear zones represent zones with negative seismic impedance [Meissner,
559 1996]. Synthetic shot gathers for a random shear zone in the uppermost mantle with 50%
560 normal peridotites and 50% material with reduced V_p [Hansen and Balling, 2004] do not
561 show scattered waves coming from it. Observations of shear zones on exposed mantle rocks
562 indicate changes in the petrophysical properties (mylonitization) [e.g. Vissers *et al.*, 1995;
563 Gómez Barreiro *et al.*, 2015; Gomez Barreiro *et al.*, 2018] that lead to a reduction in the P-
564 wave velocity. However, our analysis indicates that the observed sub-Moho reflection PM₁P
565 corresponds to a sub-horizontal reflector, featuring an increase in P-wave velocity with depth
566 and located at different levels, reinforcing the fact that it does not correspond to a shear zone.

567 The effect of fluids is probably more important in young tectonic systems, while in the
568 subcontinental mantle, fluids are limited to nominally anhydrous mineral phases [Fumagalli
569 and Klemme, 2015]. The presence of fluids in the mantle, that have zero shear modulus, can
570 also produce an impedance contrast large enough to cause reflectivity. Fluids are likely to be
571 present in subduction zones where water is introduced into the upper mantle along the upper
572 part of the subducting slab via dehydration, and/or melt is produced along the subducted slab.
573 This is not the case of the study area, where nowadays there are no active subduction
574 processes. Thus, if fluids were present in the mantle in the past, they might have migrated or
575 have been involved in mineral reactions. Another source of fluids could be the nearby
576 Calatrava Volcanic Field (Figure 1, ~N39°/W°), a Neogene volcanic field that extends over
577 5000 km² on the southeast edge of the CIZ (Figure 1). Surface wave tomography studies
578 indicate that partial melting exists underneath this field at shallow depths (65 km)
579 [Palomeras *et al.*, 2014]. Although the presence of these magmas seems obvious, it is
580 unlikely that they may inflow the lithospheric mantle of a wide area such as southwest and

581 west Iberia (Figure 8). Therefore, we consider that the presence of fluids can be ruled out as
 582 the source of the southwest Iberia upper mantle reflectivity.

583 Finally, another potential source for the target reflectivity is the presence of mafic bodies
 584 partially transformed into eclogites [e.g. *Hansen and Balling, 2004*]. Depending on the
 585 availability of water and the rock composition, mafic rocks begin to transform into eclogites
 586 at about 35 km [*Green and Ringwood, 1967a; Ito and Kennedy, 1971; Hacker, 1996*]. The
 587 eclogite/peridotite seismic contrast could result in visible reflectivity [*Chian et al., 1998;*
 588 *Wang et al., 2009; Clowes et al., 2010; Worthington et al., 2013*]. A sub-horizontal layer of
 589 mafic rocks in the mantle could have a reflection coefficient large enough to be observed in
 590 vertical incidence seismic data as a continuous bright feature, something not seen here. But
 591 field observations suggest that eclogitization could be erratic, and small bodies are
 592 commonly interbedded in peridotitic massifs [e.g. *Austrheim et al., 1997; Medaris et al.,*
 593 *2018*]. We will discuss this hypothesis in the next section.

594 6.4. An Image of the Hales Discontinuity in SW Iberia?

595 The characteristics of the PM₁P reflection observed under the western Iberian Massif suggest
 596 the existence of an increase in P-wave velocity with depth produced by a band of
 597 heterogeneities at approximately 55-85 km. Several long-range controlled source
 598 experiments imaged a positive impedance contrast boundary at 60-90 km depth [*Green and*
 599 *Hales, 1968; Hales, 1969, 1972; Hales et al., 1980*] that were interpreted as the Hales
 600 discontinuity and attributed to the spinel-to-garnet phase transition. In this section, we
 601 discuss whether the modelled PM₁P reflection could correspond to the Hales discontinuity.

602 The continental upper mantle is a complex ensemble of ultramafic and mafic rocks.
 603 Peridotites are ultramafic igneous rocks typically made of olivine (>40%), clinopyroxene,
 604 orthopyroxene and an aluminous phase (plagioclase, spinel or garnet, depending on P-T
 605 conditions [*Kushiro and Yoder, 1966; Green and Hibberson, 1970; O'Neill, 1981*]. Mafic
 606 rocks (<40% olivine) are present, though less abundant, in the upper mantle (e.g. eclogites
 607 and pyroxenites) and reflect the imprint of tectonic and magmatic processes [*Irving, 1980;*
 608 *Rudnick et al., 2000; Carlson et al., 2005*]. Among peridotites, lherzolites are very common,
 609 and represent a fertile mantle able to produce basaltic magmas [*McDonough and Rudnick,*
 610 *1998*].

611 The spinel-garnet transition is a critical reaction in the mantle. However, experimental
 612 investigations in natural compositional space are limited and incomplete [e.g. *Green and*
 613 *Ringwood, 1967b; Fumagalli and Klemme, 2015*, and references therein]. Experimental
 614 research around simple compositional systems like CMAS (CaO-MgO-Al₂O₃-SiO₂) and
 615 thermodynamic modeling have provided some constraints [*O'Neill, 1981; Perkins and*
 616 *Newton, 1981; Klemme and O'Neill, 2000; Klemme, 2004; Ziberna et al., 2013*]. Apart from
 617 pressure and temperature, garnet stability is sensitive to mantle composition. That is, for
 618 fertile peridotites, like lherzolites, the spinel-garnet transition may occur at ~45 km depth
 619 (~1.5 GPa) whereas in refractory peridotites (e.g. dunites) the transition does not occur at
 620 depths shallower than ~90 km (~3.0 GPa) [*O'Neill, 1981*]. The addition of elements like Cr
 621 and Fe has a relevant effect on the system, elevating and reducing the garnet stability
 622 pressure, respectively [*O'Neill, 1981; Girnig and Brey, 1999*].

623 Volcanic mantle xenoliths provide direct petrological and chemical information about the
 624 mantle [Pearson *et al.*, 2014]. We utilized the closest mantle xenoliths from the Late
 625 Miocene-Quaternary Calatrava Volcanic Field (CVF, Fig. 1; [Bianchini *et al.*, 2010]) to
 626 constrain the nearby mantle. In that area, lherzolites with olivine, two pyroxenes and spinel
 627 dominate. Garnet is absent in all xenoliths. Using the bulk compositions of peridotite
 628 xenoliths from Villaseca *et al.* [2010] (samples 58498 and 72672 of Cerro Pelado), and
 629 Bianchini *et al.* [2010] (sample CLV8) we explored the peridotitic parental magma pressure
 630 (P) and temperature (T) by applying thermodynamical modeling (MELTS, Ghiorso and Sack
 631 [1995]), as well as classical geothermobarometric equations of Putirka [2008] and Albaredo
 632 [1992]. Results at 100-1300°C indicate P in the range of 22-27 25 kbar (i.e. c. 65-80 km
 633 depth) and no garnet formation in the paragenesis, in line with previous estimations of the
 634 depth of xenolith extraction (ca. 70 km; Villaseca *et al.* [2010]). In a simple compositional
 635 space (CMAS+Cr; O'Neill [1981]) the stability of spinel expands over higher pressures as a
 636 function of Cr ($Cr\# = [Cr/(Cr/Al)]$). Spinel in lherzolites of the CVF depict a Cr# range = 0.09
 637 – 0.21, with a mean value ca. $Cr\# = 0.14$ [Bianchini *et al.*, 2010; Villaseca *et al.*, 2010]. For
 638 those values, the spinel-garnet transition could be expected between 21 and 24.5 kbar
 639 [O'Neill, 1981]. On the other hand, phase transition may occur in the reflectors range -
 640 between 50-85km (ca. 15-22 kbar) - only if spinel $Cr\# < 0.05$ [O'Neill, 1981]. The
 641 discrepancy between observations and experiments is somewhat to be expected. Upper
 642 mantle composition is heterogeneous, differing from simple compositional spaces, and even
 643 small elemental variations can modify the phase transition boundary [Fumagalli and
 644 Klemme, 2015]. Besides, geochemistry of the mantle below Calatrava Volcanic Field (CVF)
 645 presents a complex metasomatic imprint, tentatively related to long-term recycling of mafic
 646 rocks through an ancient subduction system (400-500 Ma; Wilson and Downes 1991;
 647 Bianchini *et al.*, 2010), thus hindering the representativeness of the results here presented.

648 The example provided above exhibits how lateral compositional changes in the upper-mantle,
 649 like elemental variation and/or fertility degree [Barbero and Villaseca, 2000; Zeck *et al.*,
 650 2007; Villaseca *et al.*, 2012, 2015] could be invoked to explain different conditions (and
 651 depth) for the spinel-garnet transition. On the other side, taking into consideration the
 652 uncertainties on mantle thermobarometry [Fumagalli and Klemme, 2015; MacGregor, 2015],
 653 xenoliths from the CVF could be close to the spinel-garnet transformation. Also, they might
 654 be recording an old subduction environment, supporting the likely existence of eclogites in
 655 the upper mantle below the OMZ-CIZ transect. These findings would correlate with the
 656 presence of eclogite relicts exhumed in the Spanish Central System from ca. 50-60 km depth
 657 (15-19 kbar; [Barbero and Villaseca, 2000; Gómez-Pugnaire *et al.*, 2003; Sánchez-Vizcaíno
 658 *et al.*, 2003; Pereira *et al.*, 2010; Villaseca *et al.*, 2015]).

659 Some authors relate the Hales discontinuity to anisotropy [Fuchs, 1983; Zhang and Lay,
 660 1993; Bostock, 1997, 1998; Levin and Park, 2000; Saul *et al.*, 2000; Musacchio *et al.*, 2004].
 661 In fact, Díaz *et al.* [1993] reported azimuthal anisotropy for the lithospheric mantle beneath
 662 the OMZ. Hence, anisotropy could play a role in the interpretation of the observed subcrustal
 663 reflectivity. Velocity anisotropy in the mantle is usually related to the preferred orientation of
 664 olivine [e.g. Nicolas and Christensen, 1987; Ismail and Mainprice, 1998]. However, the
 665 relationship of the Hales discontinuity with anisotropy is unknown, and different
 666 explanations have been proposed according to the tectonics of the area. Bostock [1997]
 667 proposed that, in the Canadian Slave Craton, this reflector could respond, among other
 668 things, to localized strain-induced anisotropy due to weakening by the phase change. On the

669 other side, *Díaz et al.* [1993] relate the lithospheric anisotropy beneath the OMZ to shear
670 zones that accommodate the strain due to the decoupling between crust and mantle. Fast
671 polarization direction on the active areas marks the direction of the present-day strain,
672 whereas in zones with no tectonic activity the lattice preferred orientation develops as a result
673 of the strain from the latest dynamic process affecting the region. Western Iberia has been
674 basically stable since the late Paleozoic, hence mantle lithospheric anisotropy must be related
675 to past events. SKS studies indicate a fast polarization in the ENE-WSW direction beneath
676 the Iberian Peninsula [*Díaz and Gallart, 2014*] in agreement with the direction of the
677 structures in the OMZ and CIZ. Anisotropy obtained by the ILIHA-DSS profiles indicates a
678 N-S fast direction for the mantle lithosphere [*Díaz et al., 1996*] although sampling is limited
679 to the direction of the profiles. Accordingly, constraints provided by anisotropic studies in
680 the area are not conclusive, in direction and in the depth where it occurs. Moreover, the
681 observed anisotropy would have an effect on velocity and travel times and probably not so
682 much in reflectivity.

683 In order to explain the observed reflections, our model defines a stochastic distribution of
684 elliptical/elongated bodies. As discussed before, this model represents a heterogeneous
685 gradient zone where the spinel-garnet phase transition (or, maybe, eclogite relics) is the
686 source of lithological heterogeneity. Tuning effects appear in reflections from layers with a
687 thickness lesser than $\frac{1}{4}$ of the wavelength of the seismic waves [*Hansen and Balling, 2004*],
688 strongly affecting the seismic wavefield and being a source of high random reflectivity. The
689 observed coda of the PM₁P arrivals on the IBERSEIS-WA shot gathers can be reproduced
690 with fine-scale elongated ellipses of heterogeneities with $\Delta V_p = \pm 0.1$ km/s [*Ayarza et al.,*
691 *2010*]. This phase has the same seismic characteristics as that observed in the ALCUDIA-
692 WA shot gathers leading us to postulate that the same pattern produces the reflectivity.
693 Therefore, we propose a model for the SW-Iberia with vertical heterogeneities between 50
694 and 150 m within a 30 km thick gradient zone that ranges from 55-85 km depth. The
695 heterogeneity bands create constructive interferences when thicknesses < 150 km and these
696 build up the observed amplitudes and coda.

697 Although the phase change from spinel-peridotite to garnet-peridotite has a low reflection
698 coefficient to explain the observed reflections [*Warner and McGearry, 1987*], layering or
699 lenses where the spinel and garnet ratio varies could account for the observed reflectivity. A
700 similar effect appears when the peridotite - eclogite pair is explored [*Chian et al., 1998*;
701 *Hansen and Balling, 2004*; *Wang et al., 2009*; *Clowes et al., 2010*; *Worthington et al., 2013*].
702 V_p ranges for both (peridotite and eclogite) overlap for a wide range of contexts, which could
703 lead to relatively low-velocity contrasts ($\Delta V_p < 1\%$) [*Kern et al., 1999*; *Mauler et al., 2000*;
704 *Brown et al., 2009*; *Wang et al., 2009*; *Worthington et al., 2013*]. At this point, the proposed
705 model demonstrates a lamellar nature of the upper mantle between 55-85 km, seismically
706 compatible with the Hales discontinuity. Whether these heterogeneities are the result of
707 either erratic spinel-garnet transformation, a long-run mixture of eclogites and peridotites or
708 both, must be settled with further investigations (e.g. V_p/V_s ; *Worthington et al., 2013*; *Farla*
709 *et al., 2017*). However, the size and position of the reflector favors an origin linked to a phase
710 transition.

711 6.5. SW Iberia Lithosphere-Asthenosphere Boundary (LAB): The PM₂P Phase

712 A deeper reflector than the PM₁P is imaged by the ALCUDIA-WA and ILIHA-DSS surveys.
 713 We postulate that this PM₂P reflector corresponds to the base of the lithosphere, the so-called
 714 LAB. Recent active source seismic studies have imaged the base of the tectonic (lithospheric)
 715 plate [*Stern et al.*, 2014] as a negative reflection coefficient interface. The seismic LAB
 716 corresponds to a decrease in velocity with depth and our study indicates that the observed
 717 PM₂P phase features negative polarity. Therefore, we modeled this arrival as an interface
 718 located at 90-100 km depth beneath the OMZ and 80-110 km depth beneath CIZ
 719 corresponding to a decrease in velocity with depth from 8.3 km/s to 8.0 km/s. In addition, the
 720 synthetic seismograms produced in this study (Figure 9) reproduce its arrival time, offset and
 721 amplitude as coming from a decrease in velocity at the proposed depths, reinforcing this
 722 interpretation.

723 Geophysical studies on surface wave tomography place the LAB at ~90 km depth beneath
 724 the OMZ, at 80-90 on the southwest CIZ and at ~70 km on the northeast CIZ [*Palomeras et*
 725 *al.*, 2017]. Differences between this study and our results are on average around 5 km
 726 although locally, to the southwest CIZ they increase up to 15 km. Discrepancies on the LAB
 727 depth obtained by different geophysical techniques have been reported [*Eaton et al.*, 2009].
 728 Surface wave tomography provides depth-velocity models that are relatively insensitive to
 729 the sharpness of the LAB, being unable to distinguish a velocity change that occurs
 730 instantaneously in depth and one occurring over tens of kilometers [*Eaton et al.*, 2009]. This
 731 conditions the definition of the LAB, which *Palomeras et al.* [2017] took as the maximum
 732 negative velocity gradient below a fast lid, which might not be necessarily the point with the
 733 maximum impedance contrast and where reflections originate. Considering the LAB as the
 734 depth to a certain absolute velocity or velocity anomaly contour, or the depth where lateral
 735 velocity variations cease, would lead to different LAB depths for the Iberian Peninsula. This
 736 could explain the discrepancies up to ~15 km obtained by surface-wave tomography analysis
 737 and the ALCUDIA and ILIHA models presented in this study.

738 Other geophysical studies using elevation, geoid and gravity data [*Palomeras et al.*, 2011],
 739 and topography and geoid data [*Torne et al.*, 2015], report similar LAB depths for the CIZ
 740 (90 km) as the ones interpreted in the wide-angle seismic profiles presented here. These
 741 studies also increase the LAB depth beneath the southwest CIZ up to 110 km depth, in
 742 agreement with the results obtained in this study. The main differences arise beneath the
 743 northeast CIZ, where *Torne et al.* [2015] report a LAB depth of 110 km whereas our model
 744 places it at 80 km depth. However, this lithospheric thinning is in agreement with the
 745 observed in the surface wave tomography results [*Palomeras et al.*, 2017]. In summary, the
 746 topography of the LAB obtained by the seismic wide-angle datasets presented in this work is
 747 in general in agreement with that obtained by other geophysical data.

748 **7 Conclusions**

749 Modeling of different refraction/wide angle seismic datasets identifies a heterogeneous upper
 750 mantle beneath the Spanish Iberian Massif, with at least two sub-Moho reflectors. The studied
 751 profiles image an upper mantle reflector, PM₁P, produced by an increase in P-wave velocity at
 752 ~55-85 km depth beneath the OMZ that shallows up to 50-60 km beneath the CIZ (Figure 8).
 753 The characteristics of this phase (coda and amplitude) indicate that it corresponds to a band of
 754 heterogeneities randomly distributed with $\Delta V_p = \pm 0.1$ km/s. Due to its depth and to geological

755 constraints, we postulate that this interface could correspond to the top of the transition from
 756 spinel to garnet lherzolite, although the existence of a heterogeneous distribution of mafic bodies
 757 (e.g. eclogites, garnetites, pyroxenites) cannot be ruled out. The randomly distributed
 758 heterogeneities would correspond to whether mechanical or chemical mixing, which led to
 759 variations on the spinel and garnet ratio (or eclogite recycling). The geometry of this interface
 760 could be due to mantle elemental changes, fertility degree and tectonothermal evolution,
 761 including compressive, extensional collapse and pervasive transcurrent regime. The interlayer
 762 spacing of this gradient zone determines its image in different datasets. The fact that the reflector
 763 is not sampled everywhere or in every dataset indicates that it is not continuous or, most
 764 probably, that it has lateral variations that modify its reflectivity depending on the characteristics
 765 of the sampling wavelet.

766 A second, deeper reflection has been observed in the shot gathers. Its reversed polarity indicates
 767 that it corresponds to a decrease in velocity with depth. Our modeling study places this
 768 discontinuity around 90 km depth beneath the OMZ. A lateral change is observed beneath the
 769 CIZ, where it is imaged at 103-110 km depth on the southeast and shallows up to 80 km depth on
 770 the northeast. Furthermore, the imaged depth of this discontinuity agrees with the LAB depth
 771 obtained for the area by other geophysical observations. This indicates that it likely corresponds
 772 to the base of the lithosphere.

773 **Acknowledgments**

774 This research was funded by the Spanish Ministry of Economy and Competitiveness CGL2016-
 775 78560-P, the Junta de Castilla y León SA065P17, IP is funded by MCIU and USal
 776 (BEAGAL18/00090). JGB appreciates financial support from ILL (1-02-232 & 1-02-163) and
 777 superb technical assistance from T. Hansen and B. Ouladiaf. JA is funded by MICINN (Juan de
 778 la Cierva fellowship - IJC2018-036074-I). The figures in this paper were generated using the
 779 public domain Generic Mapping Tools (GMT) software [*Wessel and Smith, 1995*].

780 ILIHA-DSS data is available through Iliha DSS Group (1993). IBERSEIS-WA data is available
 781 through Palomeras et al. (2009). ALCUDIA-WA data is available through Ehsan et al. (2015).
 782

783 **References**

- 784 Abramovitz, T., H. Thybo, and M. L. W. Group (1998), Seismic structure across the Caledonian
 785 Deformation Front along MONA LISA profile 1 in the southeastern North Sea,
 786 *Tectonophysics*, 288(1–4), 153–176, doi:10.1016/S0040-1951(97)00290-4.
- 787 Aki, K., and P. G. Richards (2002), *Quantitative Seismology*, 2nd ed.
- 788 Albarede, F. (1992), How deep do common basaltic magmas form and differentiate?, *J.*
 789 *Geophys. Res.*, 97(B7), 10997, doi:10.1029/91JB02927.
- 790 Alsdorf, D., L. Brown, and D. Nelson (1996), Possible upper mantle reflection fabric on seismic
 791 profiles from the Tethyan Himalaya: Identification and tectonic interpretation, *J. Geophys.*
 792 *Res.*, 101(B11), 25305–25320.
- 793 Anand, A., D. K. Bora, K. Borah, and J. Madhab Borgohain (2017), Seismological evidence of
 794 the Hales discontinuity in northeast India, *J. Asian Earth Sci.*,
 795 doi:10.1016/j.jseaes.2017.12.015.

- 796 Andrés, J., M. Schimmel, P. Ayarza, I. Palomeras, J. Diaz, and R. Carbonell (2018), Constraints
797 on the Moho beneath the Central Iberian System., in *SEISMIX*.
- 798 Andrés, J., D. Draganov, M. Schimmel, P. Ayarza, I. Palomeras, M. Ruiz, and R. Carbonell
799 (2019), Lithospheric image of the Central Iberian Zone (Iberian Massif) using Global-Phase
800 Seismic Interferometry, *Solid Earth*, 1–26, doi:10.5194/se-2019-107.
- 801 Angiboust, S., R. Langdon, P. Agard, D. Waters, and C. Chopin (2012), Eclogitization of the
802 Monviso ophiolite (W. Alps) and implications on subduction dynamics, *J. Metamorph.*
803 *Geol.*, 30(1), 37–61, doi:10.1111/j.1525-1314.2011.00951.x.
- 804 Aulbach, S., M. Massuyeau, and F. Gaillard (2017), Origins of cratonic mantle discontinuities: A
805 view from petrology, geochemistry and thermodynamic models, *Lithos*, 268–271, 364–382,
806 doi:10.1016/j.lithos.2016.11.004.
- 807 Austrheim, H., M. Erambert, and A. K. Engvik (1997), Processing of crust in the root of the
808 Caledonian continental collision zone: the role of eclogitization, *Tectonophysics*, 273(1–2),
809 129–153, doi:10.1016/S0040-1951(96)00291-0.
- 810 Ayarza, P., I. Palomeras, R. Carbonell, J. C. Afonso, and F. Simancas (2010), A wide-angle
811 upper mantle reflector in SW Iberia: Some constraints on its nature, *Phys. Earth Planet.*
812 *Inter.*, 181(3–4), 88–102, doi:10.1016/j.pepi.2010.05.004.
- 813 Azor, A., D. Rubatto, J. F. Simancas, F. González Lodeiro, D. Martínez Poyatos, L. M. Martín
814 Parra, and J. Matas (2008), Rheic Ocean ophiolitic remnants in southern Iberia questioned
815 by SHRIMP U-Pb zircon ages on the Beja-Acebuches amphibolites, *Tectonics*, 27(5),
816 TC5006, doi:10.1029/2008TC002306.
- 817 Azor, A. et al. (2019), Deformation and Structure, in *The Geology of Iberia: A Geodynamic*
818 *Approach*, edited by C. Quesada and J. T. Oliveira, pp. 307–348, Springer International
819 Publishing.
- 820 BABEL Working Group (1990), Evidence for early proterozoic plate tectonics from seismic
821 reflection profiles in the Baltic Shield, *Nature*, 348(6296), 34–38, doi:10.1038/348034a0.
- 822 Ballèvre, M. et al. (2014), Correlation of the nappe stack in the Ibero-Armorican arc across the
823 Bay of Biscay: a joint French–Spanish project, *Geol. Soc. London, Spec. Publ.*, 405(1), 77–
824 113, doi:10.1144/SP405.13.
- 825 Balling, N. (2000), Deep seismic reflection evidence for ancient subduction and collision zones
826 within the continental lithosphere of Northwestern Europe, *Tectonophysics*, 329(1–4), 269–
827 300, doi:10.1016/S0040-1951(00)00199-2.
- 828 Barbero, L., and C. Villaseca (2000), Eclogite facies relics in metabasites from the Sierra de
829 Guadarrama (Spanish Central System): P-T estimations and implications for the Hercynian
830 evolution, *Mineral. Mag.*, 64(05), 815–836, doi:10.1180/002646100549814.
- 831 Bianchini, G., L. Beccaluva, C. Bonadiman, G. M. Nowell, D. G. Pearson, F. Siena, and M.
832 Wilson (2010), Mantle metasomatism by melts of HIMU piclogite components: new
833 insights from Fe-Iherzolite xenoliths (Calatrava Volcanic District, central Spain), *Geol. Soc.*
834 *London, Spec. Publ.*, 337(1), 107–124, doi:10.1144/SP337.6.
- 835 Bostock, M. G. (1997), Anisotropic upper-mantle stratigraphy and architecture of the Slave

- 836 craton, *Nature*, 390(27 NOVEMBER), 392–395, doi:10.1038/37102.
- 837 Bostock, M. G. (1998), Mantle stratigraphy and evolution of the Slave province, *J. Geophys.*
838 *Res. Solid Earth*, 103(B9), 21183–21200, doi:10.1029/98JB01069.
- 839 Brastad, K. (1983), Petrology of eclogites within the Bjorkedalén peridotite, West Norway, *Bull.*
840 *Minéralogie*, 106(6), 751–759, doi:10.3406/bulmi.1983.7697.
- 841 Brown, D., S. Llana-Funez, R. Carbonell, J. Alvarez-Marrón, D. Martí, and M. Salisbury (2009),
842 Laboratory measurements of P-wave and S-wave velocities across a surface analog of the
843 continental crust–mantle boundary: Cabo Ortegal, Spain, *Earth Planet. Sci. Lett.*, 285(1–2),
844 27–38, doi:10.1016/j.epsl.2009.05.032.
- 845 Calvert, A. J. (2004), Seismic reflection imaging of two megathrust shear zones in the northern
846 Cascadia subduction zone, *Nature*, 428(6979), 163–167, doi:10.1038/nature02372.
- 847 Carbonell, R. (2004), On the nature of mantle heterogeneities and discontinuities: Evidence from
848 a very dense wide-angle shot record, *Tectonophysics*, 388(1–4 SPEC. ISS.), 103–117,
849 doi:10.1016/j.tecto.2004.07.025.
- 850 Carlson, R. W., D. G. Pearson, and D. E. James (2005), Physical, chemical, and chronological
851 characteristics of continental mantle, *Rev. Geophys.*, 43(1), 1–24,
852 doi:10.1029/2004RG000156.
- 853 Chian, D., F. Marillier, J. Hall, and G. Quinlan (1998), An improved velocity model for the crust
854 and upper mantle along the central mobile belt of the Newfoundland Appalachian orogen
855 and its offshore extension, *Can. J. Earth Sci.*, 35(11), 1238–1251, doi:10.1139/e98-042.
- 856 Clowes, R. M., D. J. White, and Z. Hajnal (2010), Mantle heterogeneities and their significance:
857 results from Lithoprobe seismic reflection and refraction - wide-angle reflection studies,
858 *Can. J. Earth Sci.*, 47(5), 409–443, doi:10.1139/E10-003.
- 859 Cook, F. A., A. J. Van Der Velden, K. W. Hall, and B. J. Roberts (1999), Frozen subduction in
860 Canada's Northwest Territories: Lithoprobe deep lithospheric reflection profiling of the
861 western Canadian Shield, *Tectonics*, 18(1), 1–24, doi:10.1029/1998TC900016.
- 862 Cook, F. A., R. M. Clowes, D. B. Snyder, A. J. van der Velden, K. W. Hall, P. Erdmer, and C. A.
863 Evenchick (2004), Precambrian crust beneath the Mesozoic northern Canadian Cordillera
864 discovered by Lithoprobe seismic reflection profiling, *Tectonics*, 23(2), 1–28,
865 doi:10.1029/2002TC001412.
- 866 Dias da Silva, Í., M. F. Pereira, J. B. Silva, and C. Gama (2018), Time-space distribution of
867 silicic plutonism in a gneiss dome of the Iberian Variscan Belt: The Évora Massif (Ossa-
868 Morena Zone, Portugal), *Tectonophysics*, 747–748, 298–317,
869 doi:10.1016/j.tecto.2018.10.015.
- 870 Díaz, J., J. Gallart, and R. Carbonell (2016), Moho topography beneath the Iberian-Western
871 Mediterranean region mapped from controlled-source and natural seismicity surveys,
872 *Tectonophysics*, 692, 74–85, doi:10.1016/j.tecto.2016.08.023.
- 873 Díaz, J., and J. Gallart (2014), Seismic anisotropy from the Variscan core of Iberia to the
874 Western African Craton: New constraints on upper mantle flow at regional scales, *Earth*
875 *Planet. Sci. Lett.*, 394, 48–57, doi:10.1016/j.epsl.2014.03.005.

- 876 Díaz, J., A. Hirn, J. Gallart, and L. Senos (1993), Evidence for azimuthal anisotropy in southwest
877 Iberia from deep seismic sounding data, *Phys. Earth Planet. Inter.*, 78, 193–206.
- 878 Díaz, J., A. Hirn, J. Gallart, and B. Abalos (1996), Upper-mantle anisotropy in SW Iberia from
879 long-range seismic profiles and teleseismic shear-wave data, *Phys. Earth Planet. Inter.*,
880 9201(95).
- 881 Eaton, D. W., F. Darbyshire, R. L. Evans, H. Grütter, A. G. Jones, and X. Yuan (2009), The
882 elusive lithosphere–asthenosphere boundary (LAB) beneath cratons, *Lithos*, 109(1–2), 1–
883 22, doi:10.1016/j.lithos.2008.05.009.
- 884 Ehsan, S. A., R. Carbonell, P. Ayarza, D. Martí, A. Pérez-Estaún, D. J. Martínez-Poyatos, J. F.
885 Simancas, A. Azor, and L. Mansilla (2014), Crustal deformation styles along the
886 reprocessed deep seismic reflection transect of the Central Iberian Zone (Iberian Peninsula),
887 *Tectonophysics*, 621, 159–174, doi:10.1016/j.tecto.2014.02.014.
- 888 Ehsan, S. A., R. Carbonell, P. Ayarza, D. Martí, D. Martínez Poyatos, J. F. Simancas, A. Azor,
889 C. Ayala, M. Torné, and A. Pérez-Estaún (2015), Lithospheric velocity model across the
890 Southern Central Iberian Zone (Variscan Iberian Massif): The ALCUDIA wide-angle
891 seismic reflection transect, *Tectonics*, 34(3), 535–554, doi:10.1002/2014TC003661.
- 892 Farla, R., A. Rosenthal, C. Bollinger, S. Petitgirard, J. Guignard, N. Miyajima, T. Kawazoe, W.
893 A. Crichton, and D. J. Frost (2017), High-pressure, high-temperature deformation of dunite,
894 eclogite, clinopyroxenite and garnetite using in situ X-ray diffraction, *Earth Planet. Sci.*
895 *Lett.*, 473, 291–302, doi:10.1016/j.epsl.2017.06.019.
- 896 Fernández Viejo, G., and R. M. Clowes (2003), Lithospheric structure beneath the Archaean
897 Slave Province and Proterozoic Wopmay orogen, northwestern Canada, from a
898 LITHOPROBE refraction/wide-angle reflection survey, *Geophys. J. Int.*, 153(1), 1–19,
899 doi:10.1046/j.1365-246X.2003.01807.x.
- 900 Fonseca, P., and A. Ribeiro (1993), Tectonics of the Beja-Acebuches Ophiolite: a major suture in
901 the Iberian Variscan Foldbelt, *Geol. Rundschau*, 82(3), 440–447, doi:10.1007/BF00212408.
- 902 Fountain, D. M., C. A. Hurich, and S. B. Smithson (1984), Seismic reflectivity of mylonite zones
903 in the crust, *Geology*, 12(4), 195, doi:10.1130/0091-
904 7613(1984)12<195:SRMZI>2.0.CO;2.
- 905 Fountain, D. M., T. M. Boundy, H. Austrheim, and P. Rey (1994), Eclogite-facies shear zones—
906 deep crustal reflectors?, *Tectonophysics*, 232(1–4), 411–424, doi:10.1016/0040-
907 1951(94)90100-7.
- 908 Frederiksen, S., and J. Braun (2001), Numerical modelling of strain localisation during extension
909 of the continental lithosphere, *Earth Planet. Sci. Lett.*, 188(1–2), 241–251,
910 doi:10.1016/S0012-821X(01)00323-5.
- 911 Fuchs, K. (1983), Recently formed elastic anisotropy and petrological models for the continental
912 subcrustal lithosphere in southern Germany, *Phys. Earth Planet. Inter.*, 31(2), 93–118,
913 doi:10.1016/0031-9201(83)90103-6.
- 914 Fuchs, K., M. Tittgemeyer, T. Ryberg, F. Wenzel, and W. D. Mooney (2002), Global
915 significance of a sub-Moho boundary layer (SMBL) deduced from high-resolution seismic

- 916 observations, *Int. Geol. Rev.*, *44*(8), 671–685, doi:10.2747/0020-6814.44.8.671.
- 917 Fumagalli, P., and S. Klemme (2015), Mineralogy of the Earth: Phase Transitions and
918 Mineralogy of the Upper Mantle, in *Treatise on Geophysics*, vol. 2, edited by G. Schubert,
919 pp. 7–31, Elsevier, Oxford, Oxford.
- 920 Ghiorso, M. S., and R. O. Sack (1995), Chemical mass transfer in magmatic processes IV. A
921 revised and internally consistent thermodynamic model for the interpolation and
922 extrapolation of liquid-solid equilibria in magmatic systems at elevated temperatures and
923 pressures, *Contrib. to Mineral. Petrol.*, *119*(2–3), 197–212, doi:10.1007/BF00307281.
- 924 Gurnis, A. V., and G. P. Brey (1999), Garnet-spinel-olivine-orthopyroxene equilibria in the FeO-
925 MgO-Al₂O₃-SiO₂-Cr₂O₃ system: II. Thermodynamic analysis, *Eur. J. Mineral.*, *11*(4),
926 619–636, doi:10.1127/ejm/11/4/0619.
- 927 Gómez-Pugnaire, M. T., A. Azor, J. M. Fernández-Soler, and V. López Sánchez-Vizcaíno
928 (2003), The amphibolites from the Ossa-Morena/Central Iberian Variscan suture
929 (Southwestern Iberian Massif): Geochemistry and tectonic interpretation, *Lithos*, *68*(1–2),
930 23–42, doi:10.1016/S0024-4937(03)00018-5.
- 931 Gomez Barreiro, J., S. Barrios Sanchez, J. M. Benitez Perez, Y. El Mendily, L. Lutterotti, J.
932 Morales, B. Ouladdiaf, M. Tettamanti, and M. Zucali (2018), Texture-induced anisotropy as
933 a seismic tectonic flow fingerprint, , doi:10.5291/ILL-DATA.1-02-232.
- 934 Gómez Barreiro, J., J. R. Martínez Catalán, D. Prior, H. -R. Wenk, S. Vogel, F. Díaz García, R.
935 Arenas, S. Sánchez Martínez, and I. Lonardelli (2010), Fabric Development in a Middle
936 Devonian Intraoceanic Subduction Regime: The Careón Ophiolite (Northwest Spain), *J.*
937 *Geol.*, *118*(2), 163–186, doi:10.1086/649816.
- 938 Gómez Barreiro, J., H.-R. Wenk, and S. Vogel (2015), Texture and elastic anisotropy of a
939 mylonitic anorthosite from the Morin Shear Zone (Quebec, Canada), *J. Struct. Geol.*, *71*,
940 100–111, doi:10.1016/j.jsg.2014.07.021.
- 941 Gorman, A. R. et al. (2002), Deep Probe: imaging the roots of western North America, *Can. J.*
942 *Earth Sci.*, *39*(3), 375–398, doi:10.1139/e01-064.
- 943 Green, D. H., and W. Hibberson (1970), The instability of plagioclase in peridotite at high
944 pressure, *Lithos*, *3*(3), 209–221, doi:10.1016/0024-4937(70)90074-5.
- 945 Green, D. H., and A. E. Ringwood (1967a), An experimental investigation of the gabbro to
946 eclogite transformation and its petrological applications, *Geochim. Cosmochim. Acta*, *31*(5),
947 767–833, doi:10.1016/S0016-7037(67)80031-0.
- 948 Green, D. H., and A. E. Ringwood (1967b), The stability fields of aluminous pyroxene peridotite
949 and garnet peridotite and their relevance in upper mantle structure, *Earth Planet. Sci. Lett.*,
950 *3*(C), 151–160, doi:10.1016/0012-821X(67)90027-1.
- 951 Green, R. W. E., and A. L. Hales (1968), The travel times of P waves to 30° in the central United
952 States and upper mantle structure, *Bull. Seismol. Soc. Am.*, *58*(1), 267–289.
- 953 Griffin, W. L., S. Y. O'Reilly, J. C. Afonso, and G. C. Begg (2009), The Composition and
954 Evolution of Lithospheric Mantle: a Re-evaluation and its Tectonic Implications, *J. Petrol.*,
955 *50*(7), 1185–1204, doi:10.1093/petrology/egn033.

- 956 Hacker, B. R. (1996), Eclogite formation and the rheology, buoyancy, seismicity, and H₂O
957 content of oceanic crust, in *Geophysical Monograph Series*, vol. 96, pp. 337–346.
- 958 Hajnal, Z., B. Nemeth, R. M. Clowes, R. M. Ellis, G. D. Spence, M. J. a. Burianyk, I. Asudeh, D.
959 J. White, and D. a. Forsyth (1997), Mantle involvement in lithospheric collision: Seismic
960 evidence from the Trans-Hudson Orogen, western Canada, *Geophys. Res. Lett.*, 24(16),
961 2079, doi:10.1029/97GL01958.
- 962 Hales, A. L. (1969), A seismic discontinuity in the lithosphere, *Earth Planet. Sci. Lett.*, 7(July),
963 44–46.
- 964 Hales, A. L. (1972), The travel times of P seismic waves and their relevance to the upper mantle
965 velocity distribution, *Tectonophysics*, 13(1–4), 447–482.
- 966 Hales, A. L., K. J. Muirhead, and J. R. Rynn (1980), A compressional velocity distribution for
967 the upper mantle, *Tectonophysics*, 63, 309–348.
- 968 Hammer, P. T. C., and R. M. Clowes (2004), Accreted terranes of northwestern British
969 Columbia, Canada: Lithospheric velocity structure and tectonics, *J. Geophys. Res. Solid
970 Earth*, 109(6), 1–19, doi:10.1029/2003JB002749.
- 971 Hansen, T. M., and N. Balling (2004), Upper-mantle reflectors: Modelling of seismic wavefield
972 characteristics and tectonic implications, *Geophys. J. Int.*, 157(2), 664–682,
973 doi:10.1111/j.1365-246X.2004.02217.x.
- 974 Holliger, K., and A. R. Levander (1992), A stochastic view of lower crustal fabric based on
975 evidence from the Ivrea Zone, *Geophys. Res. Lett.*, 19(11), 1153–1156,
976 doi:10.1029/92GL00919.
- 977 Iliha DSS Group (1993), A deep seismic sounding investigation of lithospheric heterogeneity
978 and anisotropy beneath the Iberian Peninsula, *Tectonophysics*, 221, 35–51.
- 979 Irving, A. (1980), Petrology and geochemistry of composite ultramafic xenoliths in alkalic
980 basalts and implications for magmatic processes within the mantle, *Am. J. Sci.*, 280(2), 389–
981 426.
- 982 Ismaïl, W. Ben, and D. Mainprice (1998), An olivine fabric database: an overview of upper
983 mantle fabrics and seismic anisotropy, *Tectonophysics*, 296(1–2), 145–157,
984 doi:10.1016/S0040-1951(98)00141-3.
- 985 Ito, K., and G. C. Kennedy (1971), An Experimental Study of the Basalt-Garnet Granulite-
986 Eclogite Transition, in *The Structure and Physical Properties of the Earth's Crust*, edited
987 by John G. Heacock, pp. 303–314.
- 988 Janák, M., N. Froitzheim, B. Lupták, M. Vrabec, and E. J. K. Ravna (2004), First evidence for
989 ultrahigh-pressure metamorphism of eclogites in Pohorje, Slovenia: Tracing deep
990 continental subduction in the Eastern Alps, *Tectonics*, 23(5), n/a-n/a,
991 doi:10.1029/2004TC001641.
- 992 Kennett, B. L. N., and E. R. Engdahl (1991), Traveltimes for global earthquake location and
993 phase identification, *Geophys. J. Int.*, 105(2), 429–465, doi:10.1111/j.1365-
994 246X.1991.tb06724.x.

- 995 Kennett, B. L. N., E. R. Engdahl, and R. Buland (1995), Constraints on seismic velocities in the
996 Earth from traveltimes, *Geophys. J. Int.*, *122*, 108–124.
- 997 Kern, H., S. Gao, Z. Jin, T. Popp, and S. Jin (1999), Petrophysical studies on rocks from the
998 Dabie ultrahigh-pressure (UHP) metamorphic belt, Central China: Implications for the
999 composition and delamination of the lower crust, *Tectonophysics*, *301*(3–4), 191–215,
1000 doi:10.1016/S0040-1951(98)00268-6.
- 1001 Klemme, S. (2004), The influence of Cr on the garnet–spinel transition in the Earth’s mantle:
1002 experiments in the system MgO–Cr₂O₃–SiO₂ and thermodynamic modelling, *Lithos*, *77*(1–
1003 4), 639–646, doi:10.1016/j.lithos.2004.03.017.
- 1004 Klemme, S., and H. S. C. O’Neill (2000), The near-solidus transition from garnet Iherzolite to
1005 spinel Iherzolite, *Contrib. to Mineral. Petrol.*, *138*(3), 237–248,
1006 doi:10.1007/s004100050560.
- 1007 Kushiro, I., and H. S. Yoder (1966), Anorthite - forsterite and anorthite - enstatite reactions and
1008 their bearing on the basalt - eclogite transformation, *J. Petrol.*, *7*(3), 337–362,
1009 doi:10.1093/petrology/7.3.337.
- 1010 Levin, V., and J. Park (2000), Shear zones in the Proterozoic lithosphere of the Arabian shield
1011 and the nature of the Hales discontinuity, *Tectonophysics*, *323*(3–4), 131–148,
1012 doi:10.1016/S0040-1951(00)00105-0.
- 1013 MacGregor, I. D. (2015), Empirical geothermometers and geothermobarometers for spinel
1014 peridotite phase assemblages, *Int. Geol. Rev.*, *57*(15), 1940–1974,
1015 doi:10.1080/00206814.2015.1045307.
- 1016 Martínez Catalan, J. R. (2011), Are the oroclines of the Variscan belt related to late Variscan
1017 strike-slip tectonics?, *Terra Nov.*, *23*(4), 241–247, doi:10.1111/j.1365-3121.2011.01005.x.
- 1018 Martínez Catalán, J. R. (2012), The Central Iberian arc, an orocline centered in the Iberian
1019 Massif and some implications for the Variscan belt, *Int. J. Earth Sci.*, *101*(5), 1299–1314,
1020 doi:10.1007/s00531-011-0715-6.
- 1021 Martínez Catalán, J. R. et al. (2007), Space and time in the tectonic evolution of the northwestern
1022 Iberian Massif: Implications for the Variscan belt, in *Memoir of the Geological Society of
1023 America*, vol. 200, pp. 403–423, Geological Society of America.
- 1024 Martínez Catalán, J. R. et al. (2019), Variscan Suture Zone and Suspect Terranes in the NW
1025 Iberian Massif: Allochthonous Complexes of the Galicia-Trás os Montes Zone (NW Iberia),
1026 in *The Geology of Iberia: A Geodynamic Approach*, edited by C. Quesada and J. T.
1027 Oliveira, pp. 99–130, Springer International Publishing.
- 1028 Martínez Poyatos, D. et al. (2012), Imaging the crustal structure of the Central Iberian Zone
1029 (Variscan Belt): The ALCUDIA deep seismic reflection transect, *Tectonics*, *31*(3), n/a-n/a,
1030 doi:10.1029/2011TC002995.
- 1031 Massé, R. P. (1987), Crustal and upper mantle structure of stable continental regions in North
1032 America and northern Europe, *Pure Appl. Geophys.*, *125*(2–3), 205–239,
1033 doi:10.1007/BF00874495.
- 1034 Mauler, A., L. Burlini, K. Kunze, P. Philippot, and J. P. Burg (2000), P-wave anisotropy in

- 1035 eclogites and relationship to the omphacite crystallographic fabric, *Phys. Chem. Earth, Part*
1036 *A Solid Earth Geod.*, 25(2), 119–126, doi:10.1016/S1464-1895(00)00020-X.
- 1037 McDonough, W. F., and R. L. Rudnick (1998), Chapter 4. MINERALOGY AND
1038 COMPOSITION OF THE UPPER MANTLE, in *Ultrahigh Pressure Mineralogy: Physics*
1039 *and Chemistry of the Earth's Deep Interior*, edited by R. J. Hemley, pp. 139–164, De
1040 Gruyter, Berlin, Boston.
- 1041 Medaris, L. G., H. K. Brueckner, Y. Cai, W. L. Griffin, and M. Janák (2018), Eclogites in
1042 peridotite massifs in the Western Gneiss Region, Scandinavian Caledonides: Petrogenesis
1043 and comparison with those in the Variscan Moldanubian Zone, *Lithos*, 322, 325–346,
1044 doi:10.1016/j.lithos.2018.10.013.
- 1045 Meissner, R. (1996), Faults and folds, fact and fiction, *Tectonophysics*, 264(1–4), 279–293,
1046 doi:10.1016/S0040-1951(96)00132-1.
- 1047 MONA LISA Working Group (1997), MONA LISA - Deep seismic investigations of the
1048 lithosphere in the southeastern North Sea, *Tectonophysics*, 269(1–2), 1–19,
1049 doi:10.1016/S0040-1951(96)00111-4.
- 1050 Morozov, I. B., and S. B. Smithson (2000), Coda of long-range arrivals from nuclear explosions,
1051 *Bull. Seismol. Soc. Am.*, 90(4), 929–939, doi:10.1785/0119990125.
- 1052 Morozov, I. B., E. A. Morozova, S. B. Smithson, and L. N. Solodilov (1998), On the nature of
1053 the teleseismic Pn phase observed on the ultralong-range profile “Quartz,” Russia, *Bull.*
1054 *Seismol. Soc. Am.*, 88(1), 62–73.
- 1055 Musacchio, G., D. J. White, I. Asudeh, and C. J. Thomson (2004), Lithospheric structure and
1056 composition of the Archean western Superior Province from seismic refraction/wide-angle
1057 reflection and gravity modeling, *J. Geophys. Res.*, 109(B3), B03304,
1058 doi:10.1029/2003JB002427.
- 1059 Nicolas, A., and N. I. Christensen (1987), Formation of Anisotropy in Upper Mantle Peridotites -
1060 A Review, in *Composition, Structure and Dynamics of the Lithosphere-Asthenosphere*
1061 *System*, edited by K. Fuchs and C. Froidevaux, pp. 111–123, American Geophysical Union.
- 1062 Nielsen, L., H. Thybo, A. Levander, and L. N. Solodilov (2003), Origin of upper-mantle seismic
1063 scattering - Evidence from Russian peaceful nuclear explosion data, *Geophys. J. Int.*,
1064 154(1), 196–204, doi:10.1046/j.1365-246X.2003.01955.x.
- 1065 O'Neill, H. S. C. (1981), The transition between spinel lherzolite and garnet lherzolite, and its
1066 use as a Geobarometer, *Contrib. to Mineral. Petrol.*, 77(2), 185–194,
1067 doi:10.1007/BF00636522.
- 1068 Palomeras, I., R. Carbonell, I. Flecha, F. Simancas, P. Ayarza, J. Matas, D. Martínez Poyatos, A.
1069 Azor, F. González-Lodeiro, and A. Pérez-Estaún (2009), Nature of the lithosphere across
1070 the Variscan orogen of SW Iberia: Dense wide-angle seismic reflection data, *J. Geophys.*
1071 *Res.*, 114(B2), 1–29, doi:10.1029/2007JB005050.
- 1072 Palomeras, I., R. Carbonell, P. Ayarza, M. Fernández, J. F. Simancas, D. M. Poyatos, F.
1073 González Lodeiro, and A. Pérez-Estaún (2011), Geophysical model of the lithosphere
1074 across the Variscan Belt of SW-Iberia: Multidisciplinary assessment, *Tectonophysics*,

- 1075 508(1–4), 42–51, doi:10.1016/j.tecto.2010.07.010.
- 1076 Palomeras, I., S. Thurner, A. Levander, K. Liu, A. Villasenor, R. Carbonell, and M. Harnafi
1077 (2014), Finite-frequency Rayleigh wave tomography of the western Mediterranean:
1078 Mapping its lithospheric structure, *Geochemistry, Geophys. Geosystems*, *15*(1), 140–160,
1079 doi:10.1002/2013GC004861.
- 1080 Palomeras, I., A. Villaseñor, S. Thurner, A. Levander, J. Gallart, and M. Harnafi (2017),
1081 Lithospheric structure of Iberia and Morocco using finite-frequency Rayleigh wave
1082 tomography from earthquakes and seismic ambient noise, *Geochemistry, Geophys.*
1083 *Geosystems*, *18*(5), 1824–1840, doi:10.1002/2016GC006657.
- 1084 Pavlenkova, N. I. (1996), General features of the uppermost mantle stratification from long-
1085 range seismic profiles, *Tectonophysics*, *264*(1–4), 261–278,
1086 doi:http://dx.doi.org/10.1016/S0040-1951(96)00131-X.
- 1087 Pearson, D. G., D. Canil, and S. B. Shirey (2014), Mantle Samples Included in Volcanic Rocks,
1088 in *Treatise on Geochemistry*, vol. 3, pp. 169–253, Elsevier.
- 1089 Pereira, M. F., A. Apraiz, M. Chichorro, J. B. Silva, and R. A. Armstrong (2010), Exhumation of
1090 high-pressure rocks in northern Gondwana during the Early Carboniferous (Coimbra-
1091 Cordoba shear zone, SW Iberian Massif): Tectonothermal analysis and U-Th-Pb SHRIMP
1092 in-situ zircon geochronology, *Gondwana Res.*, *17*(2–3), 440–460,
1093 doi:10.1016/j.gr.2009.10.001.
- 1094 Perkins, D., and R. C. Newton (1981), The compositions of coexisting pyroxenes and garnet in
1095 the system CaO-MgO-Al₂O₃-SiO₂ at 900°-1,100° C and high pressures, *Contrib. to*
1096 *Mineral. Petrol.*, *75*(3), 291–300, doi:10.1007/BF01166769.
- 1097 Putirka, K. D. (2008), Thermometers and Barometers for Volcanic Systems, *Rev. Mineral.*
1098 *Geochemistry*, *69*(1), 61–120, doi:10.2138/rmg.2008.69.3.
- 1099 Quesada, C., J. A. Braid, P. Fernandes, P. Ferreira, R. S. Jorge, J. X. Matos, J. B. Murphy, J. T.
1100 Oliveira, J. Pedro, and Z. Pereira (2019), SW Iberia Variscan Suture Zone: Oceanic Affinity
1101 Units, in *The Geology of Iberia: A Geodynamic Approach*, edited by C. Quesada and J. T.
1102 Oliveira, pp. 131–171, Springer.
- 1103 Renedo, R. N., W. O. Nachlas, D. L. Whitney, C. Teyssier, S. Piazzolo, S. M. Gordon, and H.
1104 Fossen (2015), Fabric development during exhumation from ultrahigh-pressure in an
1105 eclogite-bearing shear zone, Western Gneiss Region, Norway, *J. Struct. Geol.*, *71*, 58–70,
1106 doi:10.1016/j.jsg.2014.09.012.
- 1107 Revenaugh, J., and T. H. Jordan (1991), Mantle layering from ScS reverberations: 3. The upper
1108 mantle, *J. Geophys. Res. Solid Earth*, *96*(B12), 19781–19810, doi:10.1029/91JB01487.
- 1109 Rudnick, R. L., M. Barth, I. Horn, and W. F. McDonough (2000), Rutile-Bearing Refractory
1110 Eclogites: Missing Link Between Continents and Depleted Mantle, *Science* (80-.),
1111 *287*(5451), 278–281, doi:10.1126/science.287.5451.278.
- 1112 Sánchez-Vizcaíno, V. L., M. T. Gómez-Pugnaire, A. Azor, and J. M. Fernández-Soler (2003),
1113 Phase diagram sections applied to amphibolites: A case study from the Ossa-
1114 Morena/Central Iberian Variscan suture (Southwestern Iberian Massif), *Lithos*, *68*(1–2), 1–

- 1115 21, doi:10.1016/S0024-4937(03)00017-3.
- 1116 Saul, J., M. R. Kumar, and D. Sarkar (2000), Lithospheric and upper mantle structure of the
1117 Indian Shield, from teleseismic receiver functions, *Geophys. Res. Lett.*, *27*(16), 2357–2360.
- 1118 Shi, F., Y. Wang, H. Xu, and J. Zhang (2010), Effects of lattice preferred orientation and
1119 retrogression on seismic properties of eclogite, *J. Earth Sci.*, *21*(5), 569–580,
1120 doi:10.1007/s12583-010-0123-z.
- 1121 Silva, J. B., and M. F. Pereira (2004), Transcurrent continental tectonics model for the Ossa-
1122 Morena Zone Neoproterozoic-Paleozoic evolution, SW Iberian Massif, Portugal, *Int. J.*
1123 *Earth Sci.*, *93*(5), 886–896, doi:10.1007/s00531-004-0424-5.
- 1124 Simancas, J. F. et al. (2003), Crustal structure of the transpressional Variscan orogen of SW
1125 Iberia: SW Iberia deep seismic reflection profile (IBERSEIS), *Tectonics*, *22*(6), 1062,
1126 doi:10.1029/2002TC001479.
- 1127 Snyder, D. B. (1991), Reflections from a relic Moho in Scotland?, in *Continental Lithosphere:*
1128 *Deep Seismic Reflections. Geodynamics Series; vol. 22*, edited by O. Reilly and F. Head-
1129 clew, pp. 307–313, American Geophysical Union.
- 1130 Snyder, D. B., and A. Flack (1990), Caledonian Age Reflectors within the Mantle Lithosphere
1131 North and west of Scotland, *Tectonics*, *9*(4), 903–922.
- 1132 Sochacki, J., R. Kubichek, J. George, W. R. Fletcher, and S. Smithson (1987), Absorbing
1133 boundary conditions and surface waves., *Geophysics*, *52*(1), 60–71, doi:10.1190/1.1442241.
- 1134 Steer, D. N., J. H. Knapp, and L. D. Brown (1998), Super-deep reflection profiling: exploring the
1135 continental mantle lid, *Tectonophysics*, *286*(1–4), 111–121, doi:10.1016/S0040-
1136 1951(97)00258-8.
- 1137 Stern, T. A., S. A. Henrys, D. Okaya, J. N. Louie, M. K. Savage, S. Lamb, H. Sato, R.
1138 Sutherland, and T. Iwasaki (2014), A seismic reflection image for the base of a tectoni
1139 plate, *Nature*, *518*(7537), 85–88, doi:10.1038/nature14146.
- 1140 Stracke, A. (2012), Earth’s heterogeneous mantle: A product of convection-driven interaction
1141 between crust and mantle, *Chem. Geol.*, *330–331*, 274–299,
1142 doi:10.1016/j.chemgeo.2012.08.007.
- 1143 Taylor, G., S. Rost, and G. Houseman (2016), Crustal imaging across the North Anatolian Fault
1144 Zone from the autocorrelation of ambient seismic noise, *Geophys. Res. Lett.*, *43*(6), 2502–
1145 2509, doi:10.1002/2016GL067715.
- 1146 Thybo, H., and D. L. Anderson (2006), The heterogeneous mantle, *Tectonophysics*, *416*(1–2), 1–
1147 6, doi:10.1016/j.tecto.2005.12.002.
- 1148 Thybo, H., and E. Perchuc (1997), The Seismic 8 Discontinuity and Partial Melting in
1149 Continental Mantle, *Science (80-.)*, *275*(5306), 1626–1629,
1150 doi:10.1126/science.275.5306.1626.
- 1151 Torne, M., M. Fernández, J. Vergés, C. Ayala, M. C. Salas, I. Jimenez-Munt, G. G. Buffett, and
1152 J. Díaz (2015), Crust and mantle lithospheric structure of the Iberian Peninsula deduced
1153 from potential field modeling and thermal analysis, *Tectonophysics*, *663*, 419–433,

- 1154 doi:10.1016/j.tecto.2015.06.003.
- 1155 Villaseca, C., E. Ancochea, D. Orejana, and T. E. Jeffries (2010), Composition and evolution of
 1156 the lithospheric mantle in central Spain: inferences from peridotite xenoliths from the
 1157 Cenozoic Calatrava volcanic field, edited by M. Coltorti, H. Downes, M. Gregoire, and S. .
 1158 O'Reilly, *Geol. Soc. London, Spec. Publ.*, 337(1), 125–151, doi:10.1144/SP337.7.
- 1159 Villaseca, C., D. Orejana, and E. A. Belousova (2012), Recycled metaigneous crustal sources for
 1160 S- and I-type Variscan granitoids from the Spanish Central System batholith: Constraints
 1161 from Hf isotope zircon composition, *Lithos*, 153, 84–93, doi:10.1016/j.lithos.2012.03.024.
- 1162 Villaseca, C., P. Castiñeiras, and D. Orejana (2015), Early Ordovician metabasites from the
 1163 Spanish Central System: A remnant of intraplate HP rocks in the Central Iberian Zone,
 1164 *Gondwana Res.*, 27(1), 392–409, doi:10.1016/j.gr.2013.10.007.
- 1165 Vissers, R. L. M., M. R. Drury, E. H. H. Strating, and D. van der Wal (1991), Shear zones in the
 1166 upper mantle: A case study in an Alpine Iherzolite massif, *Geology*, 19(10), 990,
 1167 doi:10.1130/0091-7613(1991)019<0990:SZITUM>2.3.CO;2.
- 1168 Vissers, R. L. M., M. R. Drury, E. H. Hoogerduijn Strating, C. J. Spiers, and D. van der Wal
 1169 (1995), Mantle shear zones and their effect on lithosphere strength during continental
 1170 breakup, *Tectonophysics*, 249(3–4), 155–171, doi:10.1016/0040-1951(95)00033-J.
- 1171 Wang, Q., L. Burlini, D. Mainprice, and Z. Xu (2009), Geochemistry, petrofabrics and seismic
 1172 properties of eclogites from the Chinese Continental Scientific Drilling boreholes in the
 1173 Sulu UHP terrane, eastern China, *Tectonophysics*, 475(2), 251–266,
 1174 doi:10.1016/j.tecto.2008.09.027.
- 1175 Warner, M., and S. McGeary (1987), Seismic reflection coefficients from mantle fault zones,
 1176 *Geophys. J. R. Astron. Soc.*, 89(1), 223–229, doi:10.1111/j.1365-246X.1987.tb04412.x.
- 1177 Warner, M., J. Morgan, P. Barton, P. Morgan, C. Price, and K. Jones (1996), Seismic reflections
 1178 from the mantle represent relict subduction zones within the continental lithosphere,
 1179 *Geology*, 24(1), 39–42, doi:10.1130/0091-7613(1996)024<0039:SRFTMR>2.3.CO;2.
- 1180 Wilson, M., and H. Downes (1991), Tertiary - quaternary extension-related alkaline magmatism
 1181 in Western and central Europe, *J. Petrol.*, 32(4), 811–849, doi:10.1093/petrology/32.4.811.
- 1182 Worthington, J. R., B. R. Hacker, and G. Zandt (2013), Distinguishing eclogite from peridotite:
 1183 EBSD-based calculations of seismic velocities, *Geophys. J. Int.*, 193(1), 489–505,
 1184 doi:10.1093/gji/ggt004.
- 1185 Zahradník, J., P. O'Leary, and J. Sochacki (1994), Finite-difference schemes for elastic waves
 1186 based on the integration approach, *GEOPHYSICS*, 59(6), 928–937, doi:10.1190/1.1443652.
- 1187 Zand, G., and G. E. Randall (1985), Observations of shear-coupled P waves, *Geophys. Res. Lett.*,
 1188 12(9), 565–568.
- 1189 Zeck, H. P., M. T. D. Wingate, and G. Pooley (2007), Ion microprobe U–Pb zircon
 1190 geochronology of a late tectonic granitic–gabbroic rock complex within the Hercynian
 1191 Iberian belt, *Geol. Mag.*, 144(01), 157, doi:10.1017/S0016756806002652.
- 1192 Zelt, C. A., and R. B. Smith (1992), Seismic travelttime inversion for 2-D crustal velocity

- 1193 structure, *Geophys. J. Int.*, *108*, 16–34.
- 1194 Zhang, Z., and T. Lay (1993), Investigation of Upper Mantle Discontinuities Near Northwestern
1195 Pacific Subduction Zones Using Precursors To Ssh, *J. Geophys. Res. Earth*, *98*(B3), 4389–
1196 4405.
- 1197 Ziberna, L., S. Klemme, and P. Nimis (2013), Garnet and spinel in fertile and depleted mantle:
1198 insights from thermodynamic modelling, *Contrib. to Mineral. Petrol.*, *166*(2), 411–421,
1199 doi:10.1007/s00410-013-0882-5.
- 1200 Zucali, M., J. M. Benitez Perez, D. Chateigner, J. Gomez-Barreiro, L. Lutterotti, and B.
1201 Ouladdiaf (2014), Rheology of the lower crust: Quantitative Texture Analysis of High
1202 Pressure - High Temperature rocks from Alps and Iberian Variscan belt., , doi:10.5291/ILL-
1203 DATA.1-02-163.
- 1204
- 1205

1206 **Figure 1.** Tectonic map of the Iberian Peninsula with the location of the ILIHA-DSS,
 1207 IBERSEIS-WA and ALCUDIA-WA profiles (red, green and blue profiles, respectively)
 1208 analyzed in this study. The colored triangles mark the positions of the receiver stations. The
 1209 yellow stars indicate the shot positions of the wide-angle experiments. The Calatrava Volcanic
 1210 Province (CVP) is indicated by a black solid triangle. DB: Duero Basin; GB: Guadalquivir
 1211 Basin; TB: Tajo Basin; IS: Iberian System.

1212 **Figure 2.** Stacked image of the ALCUDIA-NI transect in two-way travel time (twtt), modified
 1213 after *Martínez Poyatos et al.* [2012]. Red arrows point the sub-Moho reflectors. Green arrow
 1214 depicts the lower crust-uppermost mantle tectonic wedge.

1215 **Figure 3.** Selected shot gathers from the ALCUDIA-WA experiment: shot 1 (top), shot 4
 1216 (middle), and shot 5 (bottom) (locations along the transect in Figure 1). Phases labeled in the
 1217 figure indicate the reflection and refraction at the base of the crust (PmP and Pn, respectively),
 1218 and sub-Moho reflections under study in this work (PM1P and PM2P).

1219 **Figure 4.** Frequency content of the PM1P phase for shot gathers 1 (a) and 4 (b), and PM2P for
 1220 shot gathers 4 (c) and 5 (d) of the ALCUDIA-WA experiment. All shot gathers are plotted at 8.0
 1221 km/s reduced time. Note that the dominant frequencies are lower than 20 Hz.

1222 **Figure 5.** Comparison of the polarity of the PM1P and PM2P arrivals with the PmP arrival
 1223 observed on the ALCUDIA-WA shot gathers. All shot gathers are plotted at 8.0 km/s reduced
 1224 time.

1225 **Figure 6.** a) P-wave velocity model for the ALCUDIA-WA experiment resulting from the
 1226 forward modeling. Reflectors are marked in yellow. Tectonic zones are indicated on the top of
 1227 the velocity model, colored according to figure 1. OMZ: Ossa Morena Zone, CIZ: Central
 1228 Iberian Zone, TB: Tajo Basin. Raytracing diagrams are plotted in the bottom panels on top of the
 1229 P-wave velocity model to illustrate the sampled reflectors for shot gathers 1 (b), 4 (c) and 5 (d).
 1230 Theoretical travel time branches predicted by the resulting P-wave velocity model are drawn on
 1231 top of the reduced velocity shot gathers to illustrate their alignment with the observed phases
 1232 (top panel).

1233 **Figure 7.** P-wave velocity models and subcrustal arrival times for the ILIHA-DSS experiment
 1234 resulting from the forward modeling: a) Line DA, b) Line BX, c) Line CF, and d) Line BE. Top
 1235 panels: theoretical travel time arrivals predicted by the resulting P-wave velocity model (red
 1236 dots) are plotted on top of the subcrustal arrivals (blue dots) from Iliha DSS Group [1993] to
 1237 illustrate their alignment with the observed phases. Bottom panels: Resulting P-wave velocity
 1238 models obtained in this study. Reflectors are marked in yellow. Tectonic zones are indicated on
 1239 the top of each velocity model, colored according to figure 1. SPZ: South Portuguese Zone,
 1240 OMZ: Ossa Morena Zone, CIZ: Central Iberian Zone, DB: Duero Basin, GB: Guadalquivir
 1241 Basin, BS: Betic System, IS: Iberian System.

1242 **Figure 8.** Map projection of the obtained depth of the sampled upper mantle reflectors PM1P
 1243 (left panel) and PM2P (right panel). The depth positions of the interfaces are labelled and colored
 1244 according to the depth scale. The main tectonic units are indicated (black solid lines) as in figure

1245 1. Dashed lines represent the location of the seismic lines ILIHA-DSS (red), IBERSEIS-WA
1246 (green) and ILIHA-WA (blue).

1247 **Figure 9.** a) Tectonic map of the area indicating the position of the reference P-wave velocity
1248 model (b) (black solid line) and the shot positions used for the generation of the synthetic shot
1249 gathers (d). The position of the IBERSEIS-WA Transect B and ALCUDIA-WA is also indicated
1250 as a green and blue line, respectively, as well as the shot position as yellow stars. b) Top panel:
1251 Reference P-wave velocity model for the south Iberian lithosphere created from the P-wave
1252 velocity distribution of the IBERSEIS-WA for the SPZ and OMZ, and from the ALCUDIA-WA
1253 for the CIZ. Two ~15 and ~2 km thick small-scale heterogeneity zones are included at the depth
1254 where the PM1P reflection is modeled and at the base of the crust, respectively. Velocity
1255 fluctuations are randomly distributed following a 2.7 fractal dimension with velocity variations
1256 in the range ± 0.1 km/s from the reference P-wave velocity model (bottom panel) (see text for
1257 detailed explanation). c) Field data registered by the IBERSEIS-WA Transect B and ALCUDIA-
1258 WA experiments that recorded subMoho reflectors and (d) corresponding synthetic acoustic full
1259 wave-field seismograms generated using the velocity model on b). Shot positions are labeled on
1260 a) and b). Shot gathers are plotted at a reduced velocity of 8.0 km/s. Interpreted primary phases
1261 are labeled in both real and synthetic datasets.

Figure 1.

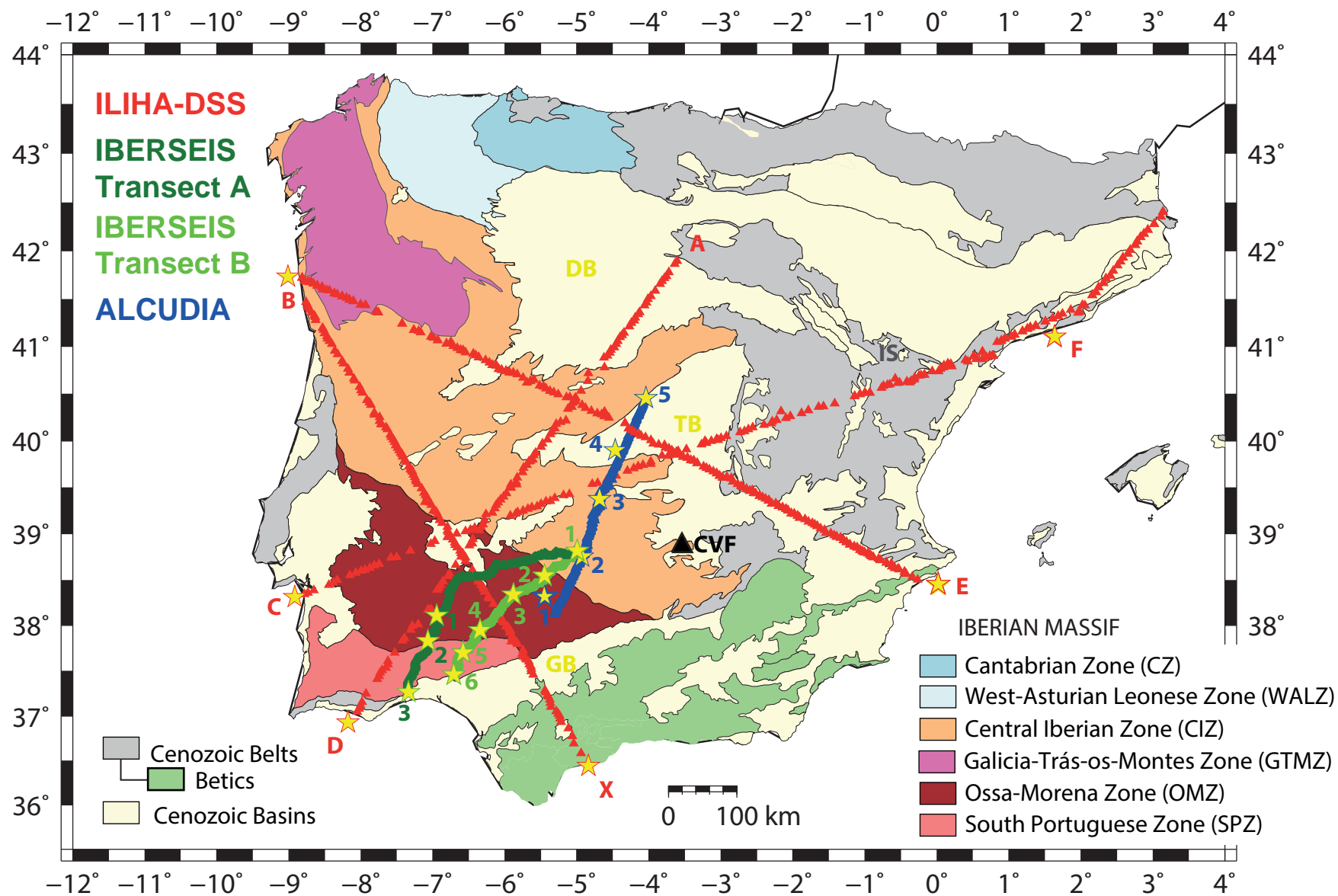


Figure 2.

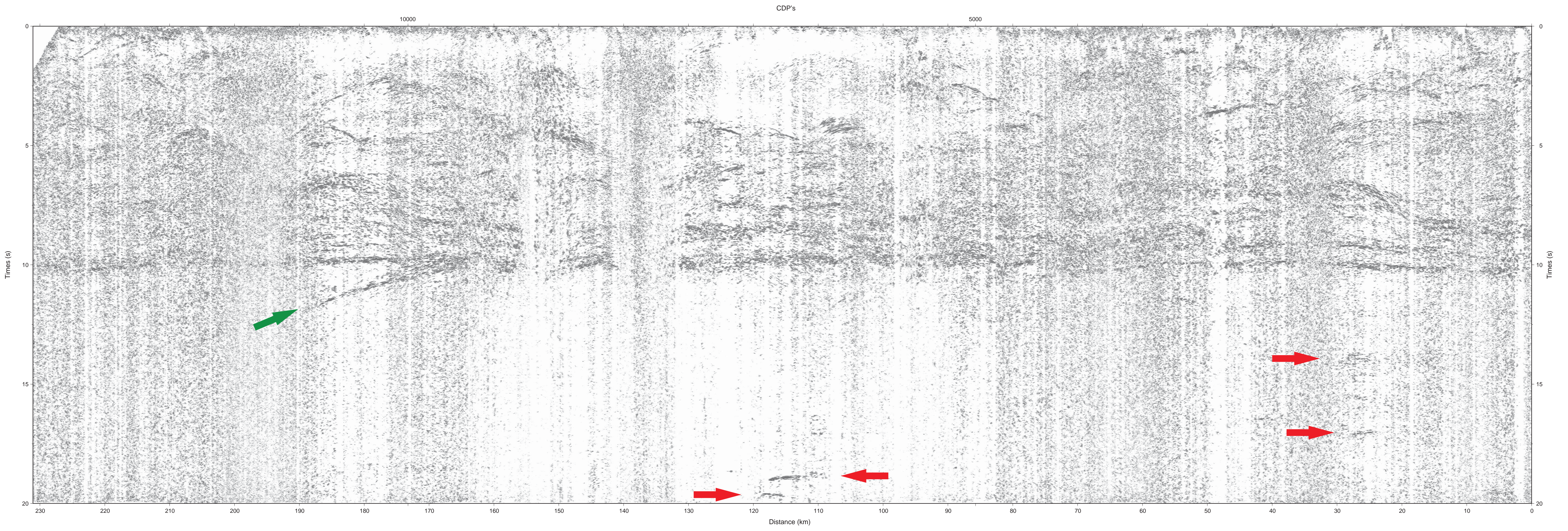


Figure 3.